# Measuring 3D Optic Nerve Head Deformations using Digital Volume Correlation of in vivo Optical Coherence Tomography Data

by

**Ziyi Zhu**

Bachelor of Science, University of Pittsburgh, 2017

Submitted to the Graduate Faculty of the

Swanson School of Engineering in partial fulfillment

of the requirements for the degree of

Master of Science in Bioengineering

University of Pittsburgh

2020

UNIVERSITY OF PITTSBURGH

SWANSON SCHOOL OF ENGINEERING

This thesis was presented

by

**Ziyi Zhu**

It was defended on

March 31, 2020

and approved by

Ian A. Sigal, Ph.D., Associate Professor, Department of Ophthalmology and Department of Bioengineering

Jonathan Vande Geest, Ph.D., Professor, Department of Bioengineering and Department of Ophthalmology

Kira L. Lathrop, MAMS, Assistant Professor, Department of Ophthalmology and Department of Bioengineering

Thesis Advisor: Ian A. Sigal, Ph.D., Associate Professor, Department of Ophthalmology and Department of Bioengineering

**Measuring 3D Optic Nerve Head Deformations using Digital Volume Correlation of in vivo Optical Coherence Tomography Data**

Ziyi Zhu, M.S.

University of Pittsburgh, 2020

The optic nerve head (ONH), located in the back of the eye, is a critical site in understanding the pathophysiology of glaucoma. However, longitudinal changes of the ONH as disease develops have not been well characterized. Our goal was to develop an improved tool to quantify these changes in an in vivo monkey model of glaucoma.

Longitudinal spectral-domain optical coherence tomography (OCT) imaging of the ONH was performed every other week under manometric intraocular pressure (IOP) control (10 mmHg) in a monkey during baseline and after induction of unilateral experimental glaucoma. We developed a computational pipeline that applied digital volume correlation (DVC) to measure the 3D ONH deformations. The chronic changes, akin to stretch, compression and shear strain were computed from OCT scans acquired in vivo at multiple stages of experimental glaucoma. Custom programs were developed to verify the robustness of the DVC algorithm and calculate a confidence map. Two regions of the ONH were segmented to focus the DVC analysis: the lamina cribrosa (LC), which plays an important role in glaucoma, and a region of the peripapillary retina, which is expected to thin through glaucoma progression.

We successfully developed a set of programs to calculate chronic tissue changes from OCT scans. We use classic DVC terminology and refer to them as displacements and strains. However, this is not exactly the case because these are long-term changes that could include deformation, and other changes such as shrinkage, growth and remodeling. The verification results of the

displacement map demonstrated high robustness of the DVC algorithm. The computed strain map suggested that chronic elevated IOP and glaucoma progression caused deformations of the ONH. The maximum chronic stretch, compression, and shear strains did not always colocalize. The LC tended to be more sensitive to chronic IOP elevation compared to the peripheral retinal nerve fiber layer. The ONH deformations did not necessarily follow the trend of chronic IOP elevation in glaucoma.

To the best of our knowledge, this is the first study to analyze the longitudinal and in vivo ONH deformations in glaucoma. Results from this study can help clarify the pathophysiology of glaucoma.

## Table of Contents

## List of Figures

## Preface

I would like to thank my adviser, Dr. Ian Sigal, for guiding me throughout the project and my colleague, Dr. Junchao Wei, who also have put great effort into this project. I would like to thank Dr. Yi Hua for providing me valuable advice and comments on the writing of this thesis. I would like to thank our collaborator, Dr. Brad Fortune, from the Devers Eye Institute for the amazing data which made this project possible. Lastly, I would like to thank everyone in the ocular biomechanics laboratory for supporting and motivating my work.

# 1.0 Introduction

Glaucoma is one of the leading causes of blindness worldwide. It poses the risk of vision loss and even blindness on over 80 million people worldwide (H A Quigley & Broman, 2006). Our lab focuses on the biomechanics of the posterior eye and aims to understand the causes of glaucoma from a mechanical perspective. Specifically, in this project, we developed a computational toolbox that employs digital volume correlation (DVC) to study chronic intraocular pressure (IOP)-induced 3D displacements and deformations of the optic nerve head (ONH). The software was used to analyze optical coherence tomography (OCT) images of monkey ONH during various time points of experimental glaucoma.

## 1.1 Structure of the Eye

The eye is composed of compliant tissues which naturally have the ability to deform (Campbell et al., 2014). The eye has an internal pressure necessary to function properly and to maintain its shape. This pressure is called IOP. The pressure is produced by a liquid inside the eye called the aqueous humor. IOP is controlled primarily by the trabecular meshwork located at the anterior part of the eye (Campbell et al., 2014), but the mechanism is complex and not completely understood.

Light comes into the eye, passing through the cornea and the lens at the anterior eye, and forms a focused image at the posterior eye. The photons are captured by the photoreceptors in the retina and, ultimately, the visual information is sent to brain by retinal ganglion cell (RGC) axons.

The visual information is transmitted by RGC axons which exit the eye through the optic disk, a small “opening” at the posterior eye also known as the ONH, and reach all the way to the brain (Sigal et al., 2012).

The ONH is one of the critical structures in the eye because all the axons must pass through it to exit the eye. Taking a closer look at the ONH, the most-anterior opening through which the axons pass is often referred to as the Bruch’s membrane opening (BMO). At the level of the sclera in this opening is a structure called the lamina cribrosa (LC). The LC is a mesh-like structure formed by collagen beams. The collagen beams in the LC are believed to provide mechanical support for the RGC axons that pass through it as well as to maintain the pressure near the opening of the eye (Jonas et al., 1992).

## 1.2 Glaucoma

Glaucoma is a disease characterized by gradual but permanent vision loss starting from the periphery of the visual field. The vision loss is due to the death of the RGC axons in the ONH, through which the eye transmits the visual information to the brain. However, the pathophysiology of glaucoma remains unclear. The main risk factor for glaucoma is the elevated IOP, often caused by blockage of the trabecular meshwork and consequently compromised drainage of the aqueous humor. However, even though a high IOP will cause glaucoma, people have vastly different susceptibility to the elevated IOP. Some people with high IOP do not develop glaucoma while some develop glaucoma despite having normal IOP (Sommer et al., 1991). The mechanisms by which a mechanical entity, namely the elevated IOP, leads to the biological effect of neural tissue damage remains poorly understood. Moreover, it is still unclear why people exhibit such a variable

sensitivity to IOP. A leading hypothesis of this for the cause of glaucoma states that the elevated IOP exerts excessive pressure on the ONH, specifically the LC, causing it to distort. The stretching and shearing of the collagen beams in the LC further result in mechanical insult to the axons within, contributing to their damage and death, and thus to glaucoma (Burgoyne et al., 2005; Campbell et al., 2014; Harry A. Quigley et al., 1983).

Besides the acute deformations in response to IOP, chronic elevated IOP can cause the remodeling of the LC (Crawford Downs et al., 2011). The remodeling of the LC progresses as glaucoma develops. This remodeling process changes the mechanical properties and the morphometry of the LC. These changes are also likely to play a role in the pathophysiology of glaucoma.

As glaucoma progresses, the thickness of the retinal nerve fiber layer (RNFL) decreases. The shrinkage of the nerve fiber layer indicates the loss of RGC axons and is correlated to visual field damage (Fortune et al., 2016). The loss of the nerve fibers can be clearly observed in OCT images and is also used by clinicians to evaluate the severity of glaucoma. Research is going on to develop and employ new techniques to extract information from OCT images and understand glaucoma.

### 1.3 Digital Volume Correlation in the Study of Glaucoma

Digital volume correlation (DVC) is a technique that tracks the voxel displacements between a reference image volume and a deformed image volume, and computes a displacement/strain map between the two volumes. Several groups have applied this technique to understand the biomechanics of the eye, as summarized below.

Sigal et al. combined digital image correlation (DIC), the 2D counterpart of DVC, with second harmonic-generated (SHG) imaging to quantify displacements and deformations of human ONH induced by acute IOP elevations. The study successfully obtained measurements of remarkable resolution that were robust to speckle noise. Results suggested that acute IOP elevations can cause substantial in-plane stretch and compression in the LC. Such deformations did not colocalize and can be highly concentrated in small regions (Sigal, Grimm, et al., 2014).

Pyne et al. developed a sequential 3D DIC approach to quantify pressure-induced deformations in the human posterior sclera. The approach enhanced the z (in-depth) resolution of standard DIC while maintaining in-plane sensitivity and is robust to the complex geometries of the ONH. The methodology offers a relatively inexpensive way to gain new insights on the ONH biomechanics and neural tissue loss (Pyne et al., 2014).

Tamimi et al. further applied the sequential DIC technique to study the racioethnic differences in human posterior pole deformations. The 3D pressure-induced deformations in the optic nerve stump (ONS), the peripapillary (PP) sclera and non-PP sclera were measured. The study quantified human ONS deformations and measured strains for all zones and regions of donors of Hispanic ethnicity. The result provided evidence that increased glaucoma prevalence in African descent and Hispanic ethnicity may have different mechanisms, and that the material properties and geometry of the ONS could be a crucial factor to consider in the analysis of scleral mechanics (Tamimi et al., 2017).

A study by Behkam et al. further advanced our understanding of ethnic differences in glaucoma by applying DVC to SHG imaging data. The authors performed pressure inflation tests on human LCs and found that eyes from donors of European Descent had significantly higher peak

shear strain in the superior quadrant of the LC compared to those of African descent and Hispanic ethnicity (Behkam et al., 2019).

Girard et al. developed a 3D tracking algorithm based on DVC to extract the displacement maps between OCT images of the reference and deformed states of the ONH. The developed algorithm was tested on artificial test cases where known displacement was applied on the reference image volume (Michael J.A. Girard et al., 2013). Based on the 3D displacement maps calculated by DVC, Zhang et al. proposed a virtual fields method to further extract the tissue mechanical properties in vivo (Zhang et al., 2017).

Feola et al. applied DVC techniques to understand the mechanical effects of cerebrospinal fluid pressure (CSFP) on the LC and the ONH. Ex-vivo images of the posterior porcine eye were acquired using phase-contrast micro-computed tomography. CSFP-induced tissue deformations were quantified using DVC. They found a huge impact of CSFP on the strain distributions in the LC and the ONH (Feola et al., 2017).

Midgett et al. applied DVC to study the pressure-induced response of human LC. The study used SHG imaging to obtain images of the LC from human donors of various ages under multiple pressures. The strains in different regions of the LC were quantified using DVC. Results suggested that the susceptibility to glaucomatous damage was linked to age-related and structure-related variations of LC strains (Midgett et al., 2017). In a more recent study by Midgett et al., DVC was applied to OCT images of human patients to understand the acute IOP-induced response of the ONH. The authors found evidence suggesting that elevated IOP caused the anterior lamina depth to be shallower and the anterior lamina cribrosa biomechanical environment to be altered (Midgett et al., 2019).

## 1.4 Specific Aims

In this project, we applied DVC techniques to study the in vivo changes of the ONH along the development of experimental glaucoma. The data we used is part of a larger data set acquired in the study by Fortune et al (Fortune et al., 2016). It is a longitudinal study on the development of experimental glaucoma where OCT scans were acquired at various time points of glaucoma progression. To the best of our knowledge, this is the first study to analyze the longitudinal and in vivo ONH deformations in the level of detail afforded by DVC. We developed a computational pipeline that allowed us to extract valuable information to understand the pathophysiology of glaucoma. Note that the displacements or deformations measured by DVC are chronic changes through the development of the disease, including not only the IOP-induced deformations, but also morphological changes such as the shrinkage of the RNFL and the remodeling of the LC.

There are two specific aims of this project:

1. Develop a computational pipeline to quantitatively measure the 3D ONH deformations
2. Evaluate the spatial and temporal trends of ONH deformations in one set of scans for one eye through the development of experimental glaucoma

# 2.0 Methods

## 2.1 Experimental Procedure

The experimental procedure and image acquisition were performed by the Fortune laboratory at the Devers eye institute in Portland Oregon. The data used in this study was a subset of the larger experiment described in more detail elsewhere (Fortune et al., 2016). For the readers' convenience, the relevant text in the method section of is reproduced below (Fortune et al., 2016).

"All procedures were performed in strict accordance with the recommendations in the Guide for the Care and Use of Laboratory Animals of the National Institutes of Health (NIH; Bethesda, MD, USA) and were approved and monitored by the Institutional Animal Care and Use Committee at Legacy Health (USDA license 92-R-0002 and OLAW assurance A3234-01). All experimental methods and animal care procedures also adhered to the Association for Research in Vision and Ophthalmology's Statement for the Use of Animals in Ophthalmic and Vision Research."

"The data used in this project is part of the data used in a previous study (Fortune et al., 2016). Briefly, this project studied a series of OCT images obtained from one eye of a female monkey, at the age of 7, along the development of experimental glaucoma, induced by applying laser photocoagulation on the trabecular meshwork. Longitudinal spectral-domain OCT (SDOCT) imaging of the ONH and peripapillary RNFL was performed every other week under manometric IOP control (10 mmHg) in a monkey during baseline and after induction of unilateral experimental glaucoma."

"The animal had five weekly baseline SDOCT imaging sessions, which are described below. Argon laser photocoagulation was applied to the trabecular meshwork of one eye of each animal to induce chronic elevation of IOP. Initially, 180° of the trabecular meshwork was treated in one session, then the remaining 180° was treated in a second session approximately 2 weeks later. If necessary, laser treatments were repeated in subsequent weeks (limited to a 90° sector) until an IOP elevation was first noted or if the initial post-laser IOP had returned to normal levels. A total of three laser treatments was applied. After initiation of laser photocoagulation, SDOCT imaging was repeated approximately every 2 weeks until euthanasia. The stage of glaucoma at euthanasia was predetermined for the animal based on the primary study to which it was assigned. Because there were four such primary studies with differing targets for postmortem histopathology, the combined cohort provided a relatively wide range of damage for the cross-sectional analysis of this study."

"All experimental procedures began with induction of general anesthesia using ketamine (10-25 mg/kg intramuscularly [IM]) in combination with either xylazine (0.8-1.5 mg/kg IM) or midazolam (0.2 mg/kg IM), along with a single injection of atropine sulfate (0.05 mg/kg IM). The animal then was intubated with an endotracheal tube to breathe a mixture of 100% oxygen, air and 1-2% isoflurane gas to maintain anesthesia to effect and oxyhemoglobin saturation as close to 100% as possible. Intravenous fluids (lactated Ringer's solution, 10-20 mL/kg/h) were administered via the saphenous vein. Vital signs were monitored throughout and recorded every 10 to 15 minutes, including heart rate, blood pressure, arterial oxyhemoglobin saturation, end-tidal CO2, and body temperature. Body temperature was maintained at 37°C, heart rate above 75 beats per minute, and oxygen saturation above 95%."

"IOP was measured in an eye at the start of every session using a Tonopen XL (Reichert Technologies, Inc., Depew, NY, USA). The value recorded for the eye was the average of three successive measurements."

## 2.2 Data Preparation

### 2.2.1 Image Acquisition

As described above in section 2.1, the experimental image acquisition was performed by our collaborators at the Devers eye institute. The details of the acquisition and other steps before analysis in this work are described elsewhere (Fortune et al., 2016). For the readers' convenience, the relevant text in the method section of this study is reproduced below (Fortune et al., 2016).

"All SDOCT scans were acquired using a Spectralis instrument (Heidelberg Engineering, GmbH, Heidelberg, Germany) 30 minutes after IOP was manometrically stabilized to 10 mmHg. This is important to minimize elastic components of deformation that are known to exert a greater effect on the ONH than on peripapillary RNFL thickness (Fortune et al., 2009; Strouthidis et al., 2011a). A clear, rigid gas permeable contact lens filled with 0.5% carboxymethylcellulose solution was placed over the apex of each cornea. SDOCT scans recorded at each session included an 80-radial B-scan pattern centered on the ONH (30° wide, 1536 A-scans/B-scan, Figure 2.1). Nine to 16 individual sweeps were averaged in real time to form each B-scan. At the first baseline imaging session, SDOCT scans were centered manually on the ONH by the operator. All follow-up scans were acquired at the same location as baseline using the instrument's automatic active eye tracking software."

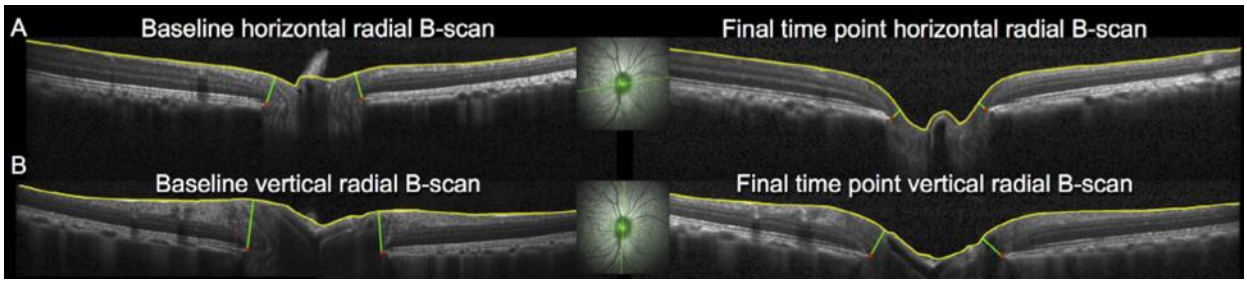


**Figure 1. "Example spectral-domain OCT scans of the ONH and peripapillary retinal nerve fiber layer. The left column shows baseline data, the right column shows final follow-up data. (A) B-scan through the horizontal meridian of the ONH. The inset shows the B-scan location indicated by the bold green line overlaid onto the infrared confocal scanning laser ophthalmoscopy (CSLO) reflectance image. Structures delineated in each radial B-scan include the inner limiting membrane (ILM, yellow) and Bruch's membrane opening (BMO) points (red). The green segments connected BMO points to the ILM. (B) B-scan through the vertical meridian of the ONH." Figure and caption reproduced from (Fortune et al., 2016).**

### 2.2.2 Image Rescaling

The raw image from OCT is not isotropic, meaning the voxel to micron ratio is not the same in each direction. This implies that the axes of the image are not in the same scale (Sigal et al., 2016). Since all the distances in the DVC computation are based on voxel distances, it is essential to make sure the images are isotropic for the program to compute deformation and strain correctly.

All images were rescaled based on the parameter settings in the OCT machine during the image acquisition. The scale in each scan direction was recorded when the image was obtained during the experiment. The z axis was aligned with the anterior-posterior, or depth, direction, with

the x and y axes perpendicular in the nasal-temporal and superior-inferior directions, respectively. The scale in the z direction is determined by the light wavelength and is generally considered constant over the scanning window. However, the scales in the x and y directions often varied between scans. For example, in the first scan, one voxel represents 5.04, 13.39 and 3.87 microns in the x, y and z directions, respectively, whereas in the second scan, a voxel represents 4.93, 13.08 and 3.87 microns, in the same directions. The images were rescaled such that all dimensions had the same voxel to micron ratio as that of the x axis. The rescaling involved interpolation, which could potentially produce artifacts. In later steps, to compensate for the effects of interpolation during rescaling we used an increased mesh density.

### 2.2.3 Image Registration

To improve the efficiency of displacement calculation (Section 2.3), we aligned the reference and deformed image volumes to minimize rigid body motion and rotation. Image registration could improve the runtime and reliability of the DVC algorithm. A custom program was developed to remove the rigid body motion semi-automatically by performing reversible linear transformations described by the following equation:

$$P_i' = C_T + R \cdot (P_i + C_s) \tag{2-1}$$

$P_i'$ : New Voxel Point $[\ x_i \quad y_i \quad z_i\ ]^T$

$P_i$ : Old Voxel Point $[\ x_i' \quad y_i' \quad z_i'\ ]^T$

$C_s$: Rotation Center $\left[\ c_x \quad c_y \quad c_z\ \right]^T$

$R$ : Rotation Tensor

The goal of the program is to calculate the rigid body displacement and rotation between the reference and deformed image volumes, and then apply the transformations to remove them. The software features an interactive window to help achieve the goal (Figure 2). The registration program allows the user to use a combination of a fast Fourier transform (FFT)-based algorithm and manual adjustment to register the two image volumes. The graphical user interface (GUI) allows the user to check the quality of image registration.

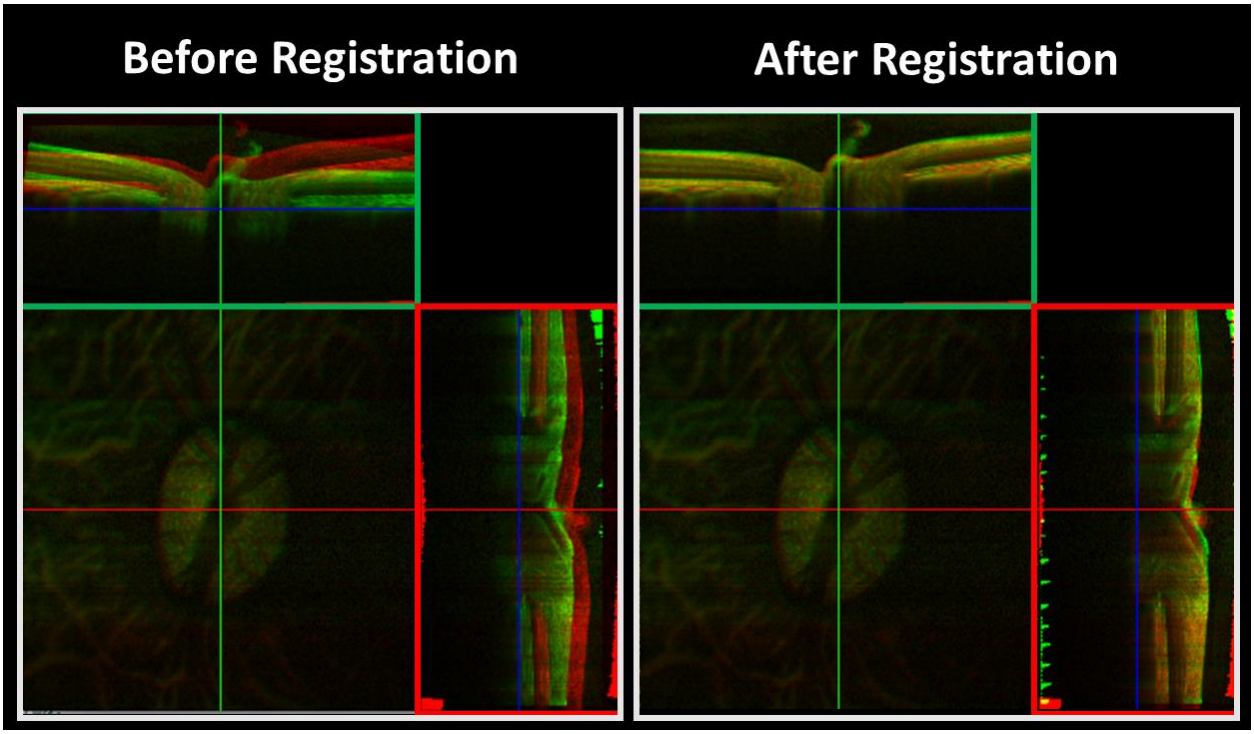


**Figure 2. Screenshots of the display of the registration program before (Left) and after (Right) registration. The input image volumes were downsized for faster processing time. The three windows in the GUI together provide an orthogonal view of the image volumes. The user is able to navigate across the image volume by moving the crosshair from each of the three windows. The display windows will show the image slices that correspond to the position of the crosshair.**

The reference (shown in red) and deformed (shown in green) image volumes were overlaid in the display window. The overlapping regions between the two image volumes were then appeared yellow. The display window shows in real time the translations and rotations applied to the images during the registration process. The GUI provides a way for visually inspecting the quality of registration and confirming that the alignment is good.

The automatic registration uses a FFT-based technique to apply translations, or rotations, to register the image volumes (Reddy & Chatterji, 1996). The phase correlation $r$ is given by the equation:

$$r = \mathcal{F}^{-1}\left\{\frac{F_1(\xi,\eta)F_2^*(\xi,\eta)}{|F_1(\xi,\eta)F_2(\xi,\eta)|}\right\} \tag{2-2}$$

where $F_1$ and $F_2$ are the Fourier transform of the reference and deformed image; $F_2^*$ is the complex conjugate of $F_2$; $\mathcal{F}^{-1}$ is the inverse Fourier transform. The translation between the reference and deformed image was computed by locating the maximum of the phase correlation. Rotation was calculated in a similar way, but the phase correlation was computed on the polar representation of the images.

The manual part of the registration allows the user to move or rotate the input image volumes from each of the three orthogonal windows to align them. This is done before the automatic registration to roughly align the input image volumes to enable better performance for the FFT-based automatic registration. The automatic registration algorithm starts from the manual registration then refines it. A crucial point to make here is that the automatic registration optimization window was large enough to allow for variations in the manual registration. Thus,

the results of the properly converged automatic registration are independent of small variations in the manual step. The manual registration was also useful when the differences between the reference and deformed image volumes were very large. Nevertheless, it is possible that in some cases the full registration may depend on the manual registration. Future work should quantify such effects. When desirable alignment is achieved, the program will scale the translation calculated on the downsized image volumes and apply it on the original image volume. The registered image volumes will then be saved for later steps.

### 2.3 Digital Volume Correlation (DVC)

To calculate the tissue deformation, a technique called digital volume correlation (DVC) was employed. DVC is a technique based on cross-correlation, which measures similarity between data, and is widely used in image registration and tracking (Bay et al., 1999; Chu et al., 1985; Michael J.A. Girard et al., 2013). Briefly, two image volumes are provided, i.e., one as a reference state and the other as a deformed state. DVC finds where a voxel in the reference volume ends up in the deformed one after deformation. This is done by evaluating which region in the deformed volume has the highest similarity with the neighbor area of the voxel we are analyzing in the reference volume. Finding such voxel pairs essentially establishes a displacement map on the reference image volume indicating how much each sampled voxel has moved after the deformation. Note that what is being measured are not displacements or strains per se, but are chronic changes through the development of experimental glaucoma, such as the IOP-induced deformations, the shrinkage of the RNFL, and the remodeling of the LC.

### 2.3.1 Sampling and Meshing

We performed random sampling and then generated meshes on the image volumes for the displacement and strain calculations. The image volumes were first passed through a median filter of size 5x5x5 voxels and a gaussian filter with sigma value of 1.8 voxels for smoothing. The smoothing parameters were chosen empirically. The potential effects of the parameter choice on the results should be carefully quantified in future work. The smoothed image was then segmented using binary thresholding. A very low threshold was used to exclude dark background with almost no signal. A morphological opening algorithm, which fills holes and joins discontinuities, was applied to the binary image to improve the segmentation of the ONH. An exact Euclidean distance transform was computed on the binary image using the SciPy library in Python (Van Der Walt et al., 2014; Virtanen et al., 2020). Distance transformation computes each voxel's shortest distance to the closest boundary and produces a greyscale image where the value at each voxel represents such shortest distance (Saito & Toriwaki, 1994).

We performed Poisson-disk sampling based on the segmented binary image and the distance-transformed matrix. It is a frequently used sampling technique in computer graphics because of the extremely desirable blue noise characteristics of its sampling distribution (Dunbar & Greg, 2004). Poisson-disk sampling produces a set of randomly sampled points that are tightly packed but are not forming clusters. This sampling method attempts to sample points as close as possible while maintaining a constraint that requires the sampled points to be at least a minimum distance apart from its neighbors. The Poisson-disk sampling was implemented based on the technique proposed in the study by Dunbar and Greg (Dunbar & Greg, 2004). The paper introduced an algorithm to implement Poisson-disk sampling with O(n) time complexity.

From the sampled points, the program creates a mesh of tetrahedron elements on the 3D image volume. Correlation and displacement were then computed based on the sampled points and mesh to reduce computational complexity.

### 2.3.2 Displacement Calculation

An original version of the code for the DVC algorithm was developed by Junchao Wei, and was reported elsewhere (Wei et al., 2018). For clarity, we summarize the most relevant steps and equations below. For the work described elsewhere in this thesis the code had to be revised and adapted to improve speed and efficiency, to allow output of the outputs of interest, and to simplify batch processing.

With the registered images, the correlation and displacement of the voxels were computed by DVC. The DVC technique measures the similarity between subsets of the reference and the deformed image using zero-normalized cross-correlation (ZNCC) (Lewis, 1995):

$$ZNCC = \frac{\sum_{X \in D}\left(f(x) - \overline{f_D}\right)\left(g(x') - \overline{g_{D'}}\right)}{\sqrt{\sum_{X \in D}\left(f(x) - \overline{f_D}\right)^2} \cdot \sqrt{\sum_{X' \in D'}\left(g(x') - \overline{g_{D'}}\right)^2}} \quad (2\text{-}3)$$

D: Reference Image Subset

D′: Deformed Image Subset

f(x): Voxel Value at x in Reference Image Subset

g(x′): Voxel Value at x′ in Deformed Image Subset

$\overline{f_D}$: Mean Value of Reference Image Subset

$\overline{g_{D'}}$: Mean Value of Deformed Image Subset

At each sampling point, a 3D search window centered at the reference sample point was constructed. The area inside this search window served as a template, which was used to find the best-match point in the deformed image volume. The best-match point in the deformed image volume was computed within the search window using template matching. The template matching algorithm finds a sub-image in the deformed image that is most similar to the template, which implies the center of this sub-image should most likely be mapped to the center of the template. The similarity was measured by the ZNCC between the sub-image and the reference template. The ZNCC represents the similarity between the center voxel in the sub-image and that in the reference template.

The template matching algorithm produces a correlation matrix that has the same size with the search window. Each entry of the correlation matrix is the calculated ZNCC value, ranging from -1 to 1, where 1 indicates a perfect match. Thus, the location where the peak correlation occurs in this correlation matrix is the best-match point that the reference voxel mapped to. Once we found where the reference point was mapped to in the deformed image, the displacement vector

at the reference point can be easily obtained by vector subtraction. Beside the displacement vectors, the maximum and mean values of the correlation matrix were also saved. These two values can give an idea of whether the mapped point in the deformed image really stands out from its neighbors in terms of similarity.

To summarize, for every sampled point on the reference image, the program computes and saves the following data: the maximum and mean values of the correlation matrix, and the displacement vector that maps the point on the reference image to its optimal matching point in the deformed image.

### 2.3.3 Strain Calculation

This part of the software computes the strain tensors at each sampling point based on the displacement map obtained in the previous step and outputs 4 parameters including the stretch, compression, shear and effective strains. As reported in section 2.3.2, the DVC code used in this section was originally developed by Junchao Wei. A comprehensive discussion on the original code can be found in this study (Wei et al., 2018). Adaptations and improvements were made to satisfy demands specific to this thesis, including automation for batch processing, better visualization and compatibility with code for later analysis. Here we summarize the appropriate discussion and reproduce the key equations presented in the original study for clarity (Wei et al., 2018).

The displacement map in the previous step can be expressed as a material transformation function in the form of:

$$\Phi(\mathrm{x}) = \mathrm{x} + \mathrm{U}(x) \approx \mathrm{x} + \mathrm{U}(\mathrm{x}_0) + \mathrm{F}(\mathrm{x}_0)(\mathrm{x} - \mathrm{x}_0) \tag{2-4}$$

$\Phi(\mathrm{x})$: Material Transformation at x

$\mathrm{x}_0$: Reference Point Vector

x: Position Vector

$\mathrm{U}(\mathrm{x}_0)$: Grid Displacement Vector $[\mathrm{u}\ \ \mathrm{v}\ \ \mathrm{w}]^{\mathrm{T}}$

$\mathrm{F}(\mathrm{x}_0)$: Deformation Gradient Tensor at $\mathrm{x}_0$: $\mathrm{F}(\mathrm{x}_0)_{\mathrm{ij}}$

$$\mathrm{F}(\mathrm{x}_0)_{\mathrm{ij}} = \begin{bmatrix} \frac{\partial \mathrm{u}}{\partial \mathrm{x}} & \frac{\partial \mathrm{u}}{\partial \mathrm{y}} & \frac{\partial \mathrm{u}}{\partial \mathrm{z}} \\ \frac{\partial \mathrm{v}}{\partial \mathrm{x}} & \frac{\partial \mathrm{v}}{\partial \mathrm{y}} & \frac{\partial \mathrm{v}}{\partial \mathrm{z}} \\ \frac{\partial \mathrm{w}}{\partial \mathrm{x}} & \frac{\partial \mathrm{w}}{\partial \mathrm{y}} & \frac{\partial \mathrm{w}}{\partial \mathrm{z}} \end{bmatrix}$$

Using a second-order interpolation method, the full-field deformation gradient was calculated from the displacement field at the matched points (Wei et al., 2018). The Lagrangian strain tensor (E) was given by the equation:

$$\mathrm{E} = \frac{1}{2}(\mathrm{F}^{\mathrm{T}}\mathrm{F} - \mathrm{I}) \tag{2-5}$$

E: Lagrangian Strain Tensor

F: Deformation Gradient Tensor

I: Identity Tensor

From the strain tensor, the stretch, compression, shear strain and the effective strain are calculated. The stretch and compression correspond to the first and third principal strains respectively. The shear and effective strains were given by the following equations:

$$E_{\max\,\text{shear}} = \frac{|P_1 - P_3|}{2} \tag{2-6}$$

$P_1$: First Principal Strain

$P_3$: Third Principal Strain

$$E_{\text{Effective}} = \sqrt{\frac{2}{3} E'_{ij} E'_{ij}}$$

$E'_{ij} = E_{ij} - \overline{E_{ij}}$: Deviatoric Strain

$\overline{E_{ij}} = \frac{1}{3}\delta_{ij} E_{kk}$: Hydrostatic Strain

The maximum shear strain is useful to understand the tearing and bending deformation, while the effective strain is a useful way to characterize in a single scalar all the components of strain (Michael J.A. Girard et al., 2013; Wei et al., 2018). After the strain calculation, the results were then mapped from the sampled points to each voxel via linear interpolation, and the strain values were visualized by creating a colormap on the 3D structural image.

## 2.4 Verification of the DVC Algorithm

### 2.4.1 Robustness of Displacement Calculation

The software provides a visual verification of the displacement map by attempting to restore the reference image from the deformed image based on the displacement map. The function maps the deformed image back to the reference state by using a spline interpolation to find the value at the mapped coordinate in the deformed image. The output is a matrix R with the same size as the reference image such that:

$$R(x, y, z) = D(x + u, y + v, z + w) \tag{2-7}$$

where x, y and z are integer coordinates and u, v and w are the components of displacement vector in the x, y and z direction. D is a spline interpolation function on the deformed image.

### 2.4.2 Confidence Evaluation

The goal of this step is to make sure we only include results that are reliable in the analysis. The DVC program will map each point in the reference image to a point in the deformed image with the highest cross correlation result. However, not every point in the mapping has the same confidence. We developed a measure of confidence at each point to evaluate how much we can trust the result and weight them before the analysis. At each point $(x, y, z)$, the confidence function was defined by:

$$\frac{C+1}{u+1} * S\left(\frac{f(x,y,z) + D(x^*, y^*, z^*)}{2}\right) \tag{2-8}$$

where $C$ and $u$ are the maximum and mean correlation of a sub-image, both range from -1 to 1, $f(x, y, z)$ is the voxel value at $(x, y, z)$ in the reference image, $D(x^*, y^*, z^*)$ is the voxel value at the corresponding voxel in the deformed image, $S$ is a sigmoid function that ranges from 0 to 1. The first term of the product accounts for how confident we are about the mapping at a given point relative to other candidate points. The value is high when the peak correlation stands out from the correlation of its neighbors. The second term accounts for the quality of image at a specific point. The rational is that even if the DVC algorithm deemed the mapping as accurate, the voxel value itself may not be reliable in the first place. OCT signal penetration and how deep into the ONH it is still possible to discern structures reliably is an important consideration (Michäel J.A. Girard et al., 2015; Sigal, Wang, et al., 2014). Noise, scattering, absorption, particularly by blood, and other effects decrease this depth. This is important as it may preclude reliable analysis of the LC.

Interestingly, in humans, it has been shown that LC visualization is better in eyes with glaucoma than in healthy eyes (Lucy et al., 2017). This is thought to be primarily due to decreased prelaminar neural tissue thickness. To evaluate the signal penetration in our scans we assessed the visibility of LC trabecular structure in coronal cross sections of the stack. We were able to see consistently this structure up to 200 μm into the LC. In some scans visibility was deeper, but a fair comparison requires us to limit the analysis to the same region. According to histomorphometric studies of monkey LC (Yang et al., 2007), 200 μm should be enough to visualize the entire LC thickness in a majority of animals, and is thus sufficient for the purpose of this study although it is possible that we missed some deeper part of the LC. Nevertheless, there still are regions, mainly in the peripheral canal and behind vasculature with poor signal penetration due to shadows casted by the blood vessels. Voxels in these regions do not provide much information regardless of their correlations. So, in addition to evaluating the correlation matrix, we normalized the confidence at a voxel with its intensity value. Such normalization was reflected by the second term of the product, which is the intensity value of that voxel mapped to 0 and 1 with a sigmoid function. The result from the DVC computation is not perfect. However, the measure of confidence allows us to still make valid analysis by excluding the data that we don't trust.

The strain data were weighted based on the confidence score. Specifically, the confidence was first normalized by the 97.5 percentile, which eliminates the effects of potential outliers caused by division, resulting in a confidence metric that range from 0 to 1. A weighted histogram was constructed based on the confidence metric. The weighting was applied in a way that when adding a value to a bin, instead of incrementing the count by one, the count was incremented by the value of the confidence.

One side effect of this weighting method is that the strain data was essentially discretized where the number of levels is the number of bins. As the strain typically ranges from 0 to 0.15, a bin count of 2000 was used to sufficiently preserves the precision. The weighted strain data was then reconstructed from the histogram using the mid-points of the edges and the bin count. Finally, the weighted strain data was visualized using both box plots and ridge plots to illustrate both the descriptive statistics and the actual distribution.

## 2.5 Regions of Interest

Having obtained the 3D strain data for the OCT volumes, the next step is to analyze these data to gain insights on the process of experimental glaucoma. It is more interesting to look at the deformation distribution by structure. To only include certain regions of the image in the analysis, markings were performed to create masks for structures of interest. For the purpose of this project, masks for two regions were obtained: The lamina cribrosa (LC) and the peripheral retina nerve fiber layer (RNFL).

### 2.5.1 Lamina Cribrosa (LC)

The LC was marked using FIJI (Rueden et al., 2017; Schindelin et al., 2012). The lamina region was manually marked on B-scans in each reference image volume that was processed by the DVC algorithm. This eliminates the need for additional processing and translation before applying on the strain data. The binary masks of the region selections were then combined to construct a 3D binary mask that indicates the lamina region in the 3D OCT image volume.

### 2.5.2 Peripheral Retinal Nerve Fiber Layer (RNFL)

Peripheral RNFL was computed from the inner limiting membrane (ILM), the nerve fiber layer (NFL) delineation and the BMO best fit plane (Figure 3). RNFLV was presented in the study by Nicholas et al (Strouthidis et al., 2011b). Briefly, the BMO, ILM and NFL were delineated in the previous study (Fortune et al., 2016). A program was developed to read the custom formatted delineation files. The delineation consists of the coordinates of the marked structures. These coordinates were transformed to match the output image after the DVC computation. For example, the x, y and z coordinates in the raw delineation data were re-scaled to match those of the isotropic image, and the translations and rotations were applied to match the registration performed by the DVC algorithm.

The ILM and NFL surface were reconstructed from the delineation using linear interpolation. The BMO best fit plane, as well as its normal vector were computed from the BMO marking using principle component analysis. A binary mask was then constructed based on these criteria and applied to the data volumes to select the points that are in the peripheral RNFL.

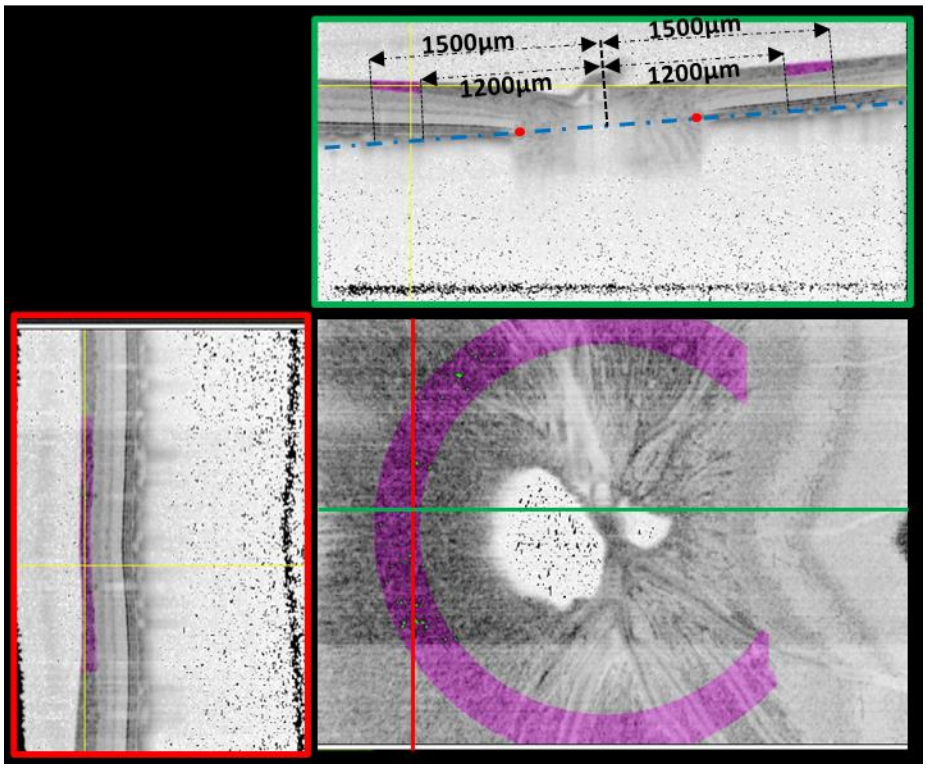


**Figure 3. Orthogonal view of the peripheral RNFL segmentation (purple). The segmentation is shown on an inverted OCT image for better visualization of the structure. Top: The two red dots represent the ends of the Bruch's membrane opening (BMO). The blue dashed line represents the BMO best-fit plane. The peripheral RNFL is defined as the area in between the ILM and NFL and in between 1200 and 1500 µm from the normal vector of the BMO plane at the center of the canal. Bottom right: The missing part of the purple ring is because the peripheral RNFL extends to the anterior and does not fall in this horizontal section.**

## 2.6 Acknowledgement of Contribution

This thesis was done within the overall envelope of a collaboration between the Sigal lab (the Laboratory of Ocular Biomechanics at the University of Pittsburgh) and the Fortune lab (at the Devers eye institute). The contributions to this project were as described below.

The experimental procedure and image acquisition were performed at the Devers eye institute by the Fortune lab. This thesis used a subset of the data from the Fortune lab (Fortune et al., 2016).

The computational pipeline was fully custom-developed but has made heavy use of open-source libraries such as Scipy (Virtanen et al., 2020) and Scikit-image (Van Der Walt et al., 2014). The software development was a collaborative effort of Junchao Wei and Ziyi Zhu, both affiliated to the Laboratory of Ocular Biomechanics, University of Pittsburgh. The DVC algorithm was developed initially by Junchao Wei. Specifically, developments made by Junchao Wei include code for image rescaling, image registration, the DVC algorithm and the strain calculation. Developments made by Ziyi Zhu include a wrapper program that automatically applies DVC to perform displacements and strain calculations on a batch of images, improvements to the visualization program that illustrates 3D results calculated by DVC, a sub-module of the DVC algorithm that calculates the confidence described in section 2.4.2, code that produces 3D masks of the RNFL from delineations of the ONH structures, code that produces 3D masks of the LC from manual markings and the corresponding marking protocol, code that applies 3D masks to segment results by regions and structures, code that applies confidence weighting and visualizes the weighted distributions.

The processing of the data and the analysis of the results were performed by Ziyi Zhu. Specifically, this includes designing the analysis, testing the code and trouble-shooting any

unwanted behaviors, performing the procedures described from section 2.2.2 to 2.5.2 and creating appropriate visualizations of the results.

# 3.0 Results

## 3.1 Intraocular Pressure (IOP) History

Three laser photocoagulation sessions were done to the monkey eye at different dates. We obtained 3D deformation maps for a series of 17 OCT scans (16 pairs) during the course of experimental glaucoma development. IOP was measured prior to each OCT scan (Figure 4).

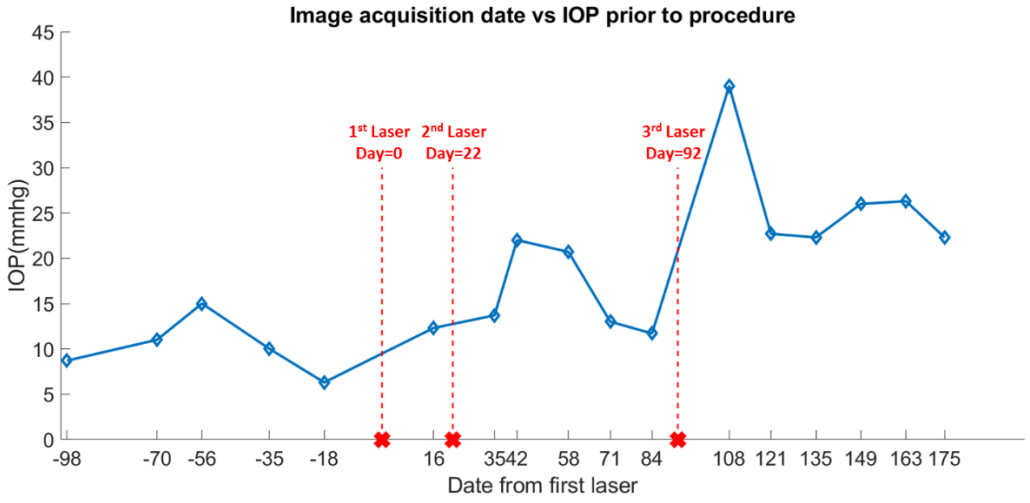


**Figure 4. IOP history. Shown are the scan dates and the mean IOP on that day. Remember that this is the pressure measured before the image acquisition and reflects the effect of experimental glaucoma on IOP. IOP during the imaging session was always brought down to 10 mmHg. The deformations were measured in a step-wise manner, i.e., the deformation in a given date is the analysis between that date and the previous one. In later discussions, we will refer to the strain as the date of the later scan in each pair, day 16 refers to the deformation between scans on day -18 and day 16, etc.**

## 3.2 DVC Algorithm Verification

The displacement map computed by our DVC algorithm was promising. Example verification results are shown in Figure 5. The original and the restored reference images were shown in red and green, respectively, resulting in the overlaid region appearing yellow. This method provides a visual verification of the displacement map. Our verification results show good qualities of the displacement mapping, as suggested by the large fraction of the yellow region. For the verification results of other scans, we refer the reader to the appendix of the thesis.

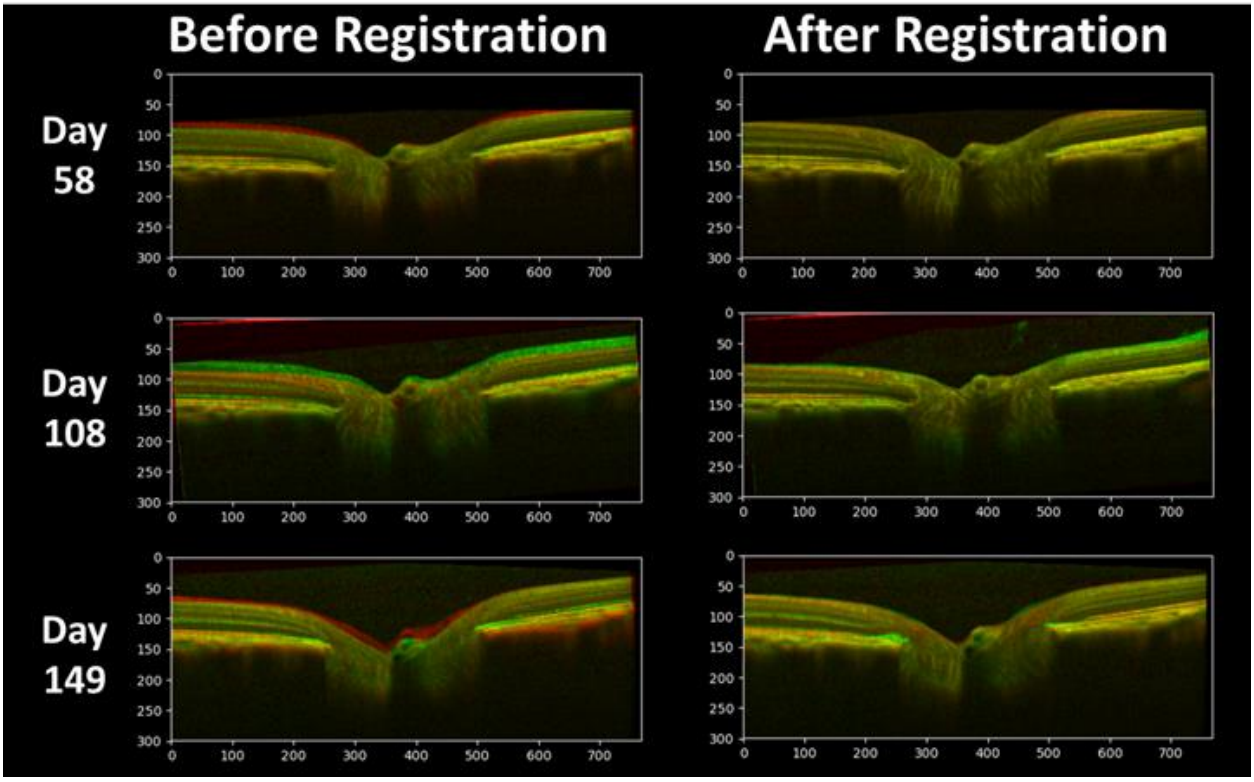


**Figure 5. Demonstration of the robustness of our DVC algorithm. Left: Reference overlaid with the deformed image (red: reference, green: deformed, yellow: match). Right: Reference overlaid with the restored image from the deformed image. (red: reference, green: restored, yellow: match) Basically, either red or green means that the images are different or that tissues do not overlap. If the images were identical and the registration was perfect, all pixels would be yellow. Axes are labeled in pixels.**

### 3.3 Strain Computation and Analysis

Figure 6 shows the stretch, compression and shear strain within the ONH at a subset of five example dates. Through the course of the glaucoma development, the tissue response was more prominent (i.e., larger strains) in scans immediately after the laser treatment (Days 16 and 108) and stabilized afterwards. Large compression was observed in Day 108, which is the scan after the third laser treatment. The maximum stretch, compression, and shear strain did not always colocalize. For the strain maps at other time points, we refer the reader to the appendix of the thesis.

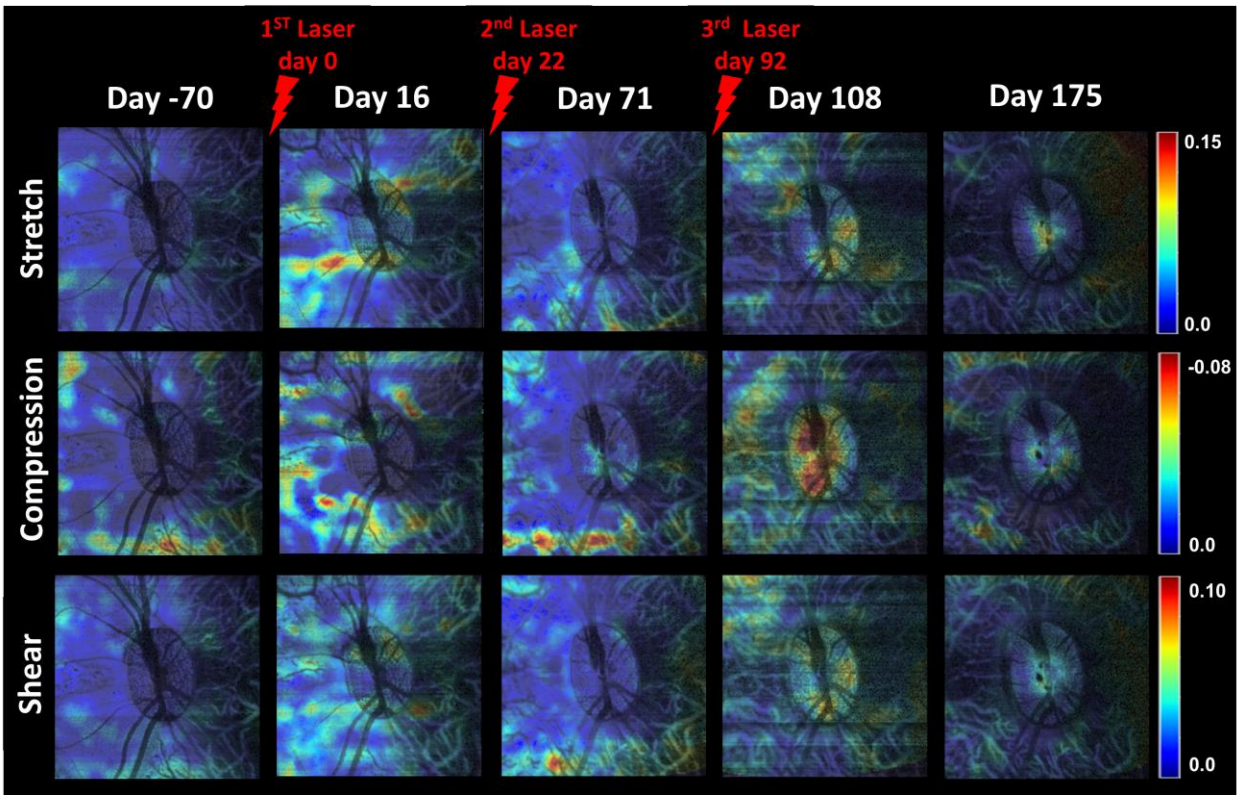


**Figure 6. Stretch, compression and shear strain within the ONH at a subset of five example dates. Rows represent the type of strain, and columns represent the time point of the scan. A plot in a given date is the analysis between that date and the previous one. Laser surgery was performed on Days 0, 22 and 92, and is marked in red. Larger strains were observed in scans immediately after the laser treatment (Days 16 and 108) and stabilized afterwards. The maximum stretch, compression, and shear strain did not always colocalize.**

We then further quantified the detailed strain distribution in two regions of interest: 1) lamina cribrosa, and 2) peripheral RNFL. The results are shown in Figure 7. Note that the strains were weighted based on the confidence level, with the methods described in Section 2.4.2.

*Lamina cribrosa*. The stretch, compression and shear strain generally followed the same trend as the effective strain, but with several notable differences. For example, in Day -18, the 50th percentile stretch was similar to that in Days -70, -56, and -35; however, the 95th percentile stretch was much larger. In Days 16 and 149, the compression was considerably lower than the other strains. In Day 84, the stretch was much larger than the compression and shear strain. In general, the strain in the LC spikes after the laser treatment and gradually settles down in the subsequent scans. The effective strain shows that in the LC region, large deformation happened in Days 16 and 108, which agrees with the date of the first and third laser treatment. However, high strain also presented in Days -18 and 84, prior to the first and third laser treatment.

*Peripheral RNFL*. The strains in the peripheral RNFL also tend to be high after the laser treatment and decrease afterwards. However, the peripheral RNFL did not appear to have the identical trend as that of the LC. The strains in the peripheral RNFL are relatively insensitive to IOP variations and fluctuate less across scans compared to that of the LC. Besides the high strain in Day 16, there was also a notable spike at Day 84, which was a period right before the third laser treatment.

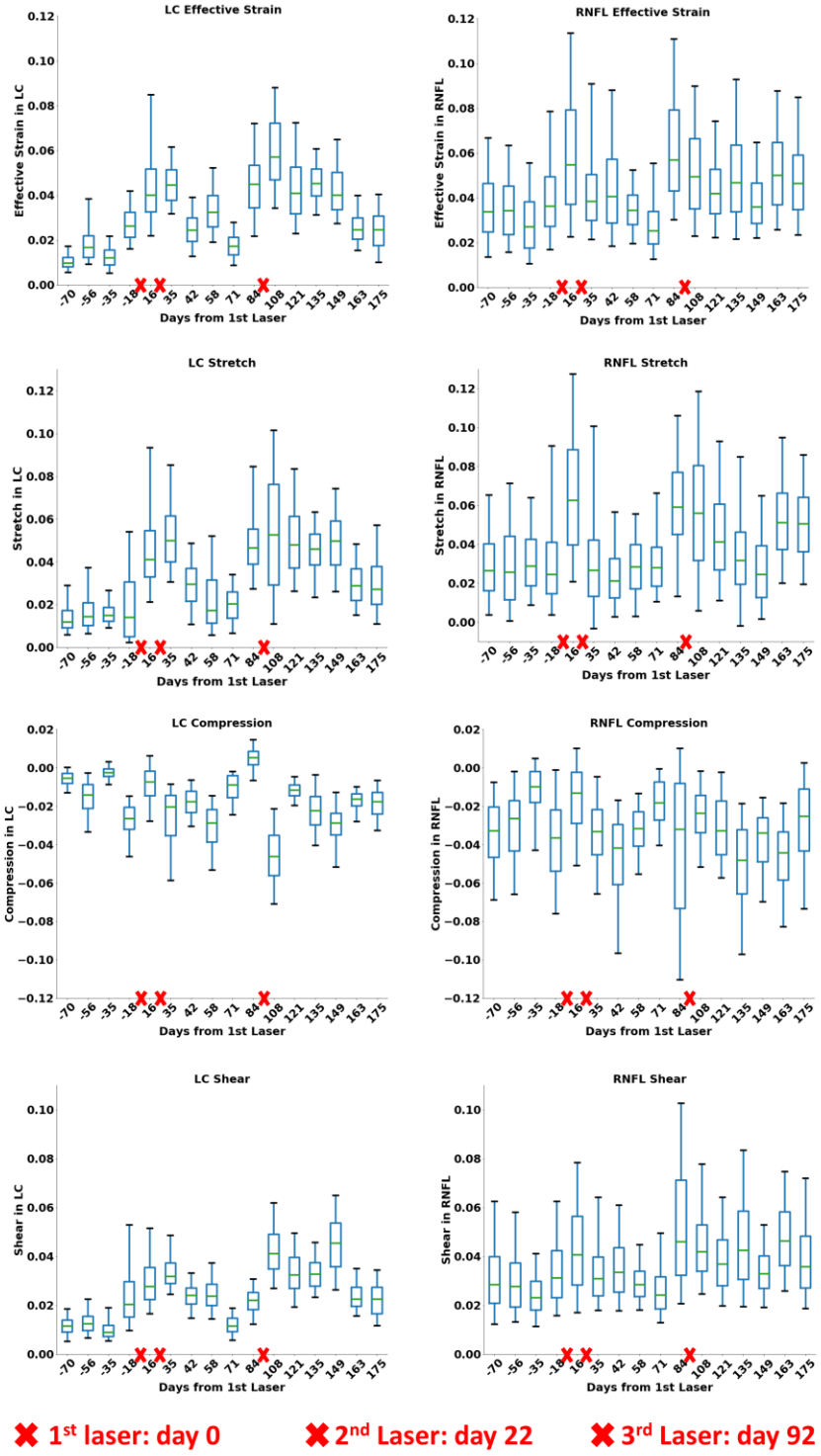


**Figure 7. Box plots of the strain distributions in the lamina cribrosa (left column) and peripheral RNFL (right column). Rows 1-4 represent the effective strain, stretch, compression and shear strain. The strain in a given**

**date is the analysis between that date and the previous one. Laser surgery was performed on Days 0, 22 and 92, and was marked by the red crosses. In general, the strains are higher after the laser treatment. The strain variations in the LC are larger than those in the peripheral RNFL, suggesting that the LC deformation is more sensitive during the progression of experimental glaucoma.**

Figure 8 shows a ridge plot of the effective strain in the LC. The ridge plot shows the detailed distribution of the box plot, which can provide a more comprehensive visualization of the strain distribution. In addition, the ridge plot allows us to examine whether it is appropriate to visualize the distributions with box plot. For example, if data follows a bimodal distribution, the box plot could be misleading. For the ridge plots of the other strains in the LC and peripheral RNFL, we refer the reader to the appendix of the thesis.

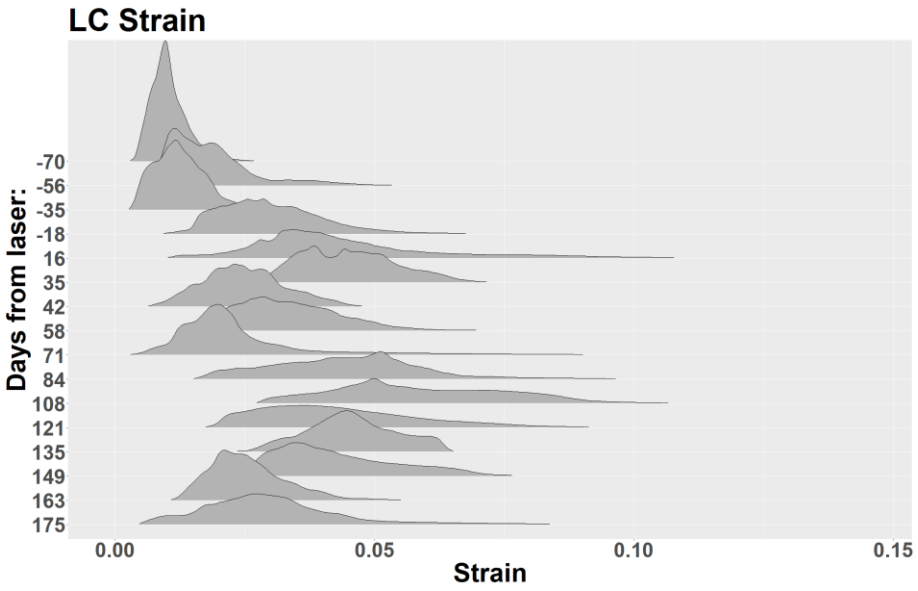


**Figure 8. Ridge plot of the effective strain in the LC. The shapes of the strain distributions vary, but are reasonably well behaved. This suggests that the box plots of the effective strain in the LC are reasonable.**

## 4.0 Discussion

Our goal was to develop an improved tool that would allow quantifying the longitudinal changes in an in vivo monkey model of experimental glaucoma. To achieve this goal, we developed a computational pipeline to quantitatively measure the 3D ONH deformations through the development of experimental glaucoma, and obtained promising results. The chronic effective strain, stretch, compression and shear strain were computed on the 3D OCT image volumes for one eye. Furthermore, segmentation of the LC and the peripheral RNFL were obtained and region-specific analysis of the strains was then performed. We evaluated the spatial and temporal trends of ONH deformations through the development of experimental glaucoma. Note that what is being measured are not displacements or strains per se, but are chronic changes through the development of experimental glaucoma, such as the IOP-induced deformations, the shrinkage of the RNFL, and the remodeling of the LC.

### 4.1 Robustness of the Verification Algorithm

The qualitative verification results suggest that our program is robust to process the OCT images and compute displacements and strains in consecutive scans. During the testing of the software, the verification algorithm is able to detect situations where the DVC program cannot correctly compute the deformation map (Figure 9). Problems could happen when the deformation is too large and exceeds the maximum searching area or when there is a large shadow area caused by blood vessels. Due to this constraint, we computed the stepwise deformations, i.e., between

each scan and its previous scan, instead of the accumulative deformations, i.e., relative to the first scan (baseline). This allows us to achieve good verification results for all inputs.

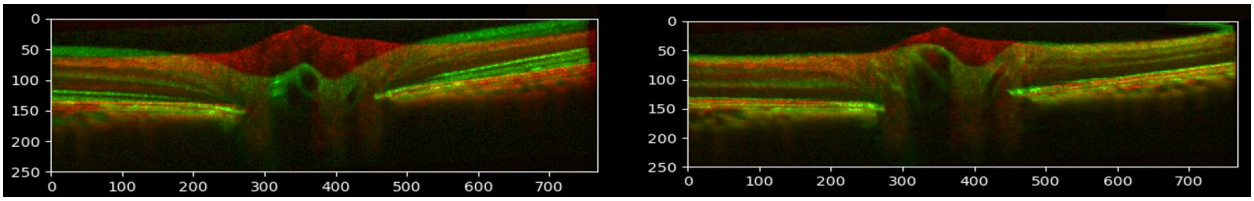


**Figure 9. Demonstration of the robustness of the verification program. Left: Reference overlaid with the deformed image (red: reference, green: deformed, yellow: match). Right: Reference overlaid with the restored image from the deformed image. (red: reference, green: restored, yellow: match) The mismatch (i.e., large red area) represents the inaccurate displacement calculations by the DVC algorithm.**

## 4.2 Robustness of the DVC Algorithm

It is worth noting that the comparison of the strains between the LC and peripheral RNFL also serves as a validation of the DVC algorithm. Although the interquartile range of the strain distributions in the peripheral RNFL is generally larger compared to that in the LC, the differences across the scans are relatively small, suggesting the peripheral RNFL is a relatively stable site compare to the LC. This agrees with our expectation from previous studies (Strouthidis et al., 2011a). The peripheral RNFL can be considered, in some sense, a control group which illustrates how the strain results would look like in a region where deformations were small. Mostly the

apparent compressions are associated with RGC axon loss. This is important because the accuracy of our DVC algorithm will always be limited by the quality and the visibility of the OCT image volumes. We employed a confidence metric to exclude data with low reliability, but it is not a guarantee that the calculated strain distribution is accurate. For the peripheral RNFL, the strain distributions, except in a few scans acquired near the date of surgeries, are reasonably normal and have similar median and interquartile range. The LC strains, on the other hand, have shown more changes as glaucoma develops. Compared to the strains in the peripheral RNFL, we argue with more confidence that the characteristics we observed are real and LC specific.

### 4.3 Strain Responses of the LC and Peripheral RNFL

The deformation in the LC and RNFL follows a similar trend. The strain changes started soon after the laser treatment and such deformation reduced gradually afterwards. Note that IOP was brought down to a normal level prior to the image acquisition. This ensures that the deformation we captured was the chronic response of tissue to persistent high pressure instead of the elastic deformation due to acute pressure changes.

Interestingly, the time period with high IOP does not necessarily correspond to the high strain. For example, from Days 40 to 60, we observed sustained IOP elevation, but the strains in the LC and peripheral RNFL were relatively low and stable. It is not clear yet what is the relation between chronic IOP elevations and mechanical deformations. However, the mismatch between IOP elevation timing and tissue deformation provided evidence that chronic IOP elevations may have different impact with acute IOP elevations and we need to make careful consideration when interpreting the results.

We noticed that high deformation happened in both LC and the peripheral RNFL on day 84, the last scan before the third laser, on which IOP was still relatively low. We don't yet have a full explanation to this. However, here we propose a potential explanation. Prior to day 84, we observed a decrease in IOP that started on day 71, after a period of high IOP. There could be some underlying physiological changes during this period that caused this IOP reduction and as well caused the large deformations on day 84.The retinal nerve fiber layer thickness is a biomarker of glaucoma. Although visual impairment only happens after a considerable amount of neural axons is lost, the axonal loss is irreversible. Due to such irreversibility, a way early detection of glaucoma is valuable. Several studies have suggested that the LC is the site where the axonal damage in glaucoma initiates, and it is critical to understand the chronic changes within the LC (Balaratnasingam et al., 2014; Yang et al., 2015). Deformation and remodeling of the LC were observed in histology of glaucomatous tissue (Burgoyne et al., 2004; Yang et al., 2007). In this project, we were able to detect in vivo LC deformations along the progression of glaucoma. From our results, we found that the increased strain in the LC happened at Day 16, following the increase of IOP. Our results demonstrate that the LC deformation happens early in glaucoma, before the loss of neural tissue and peripheral vision.

## 5.0 Conclusions

In this project, we successfully demonstrated a set of computational tools to extract 3D chronic deformations from in vivo SD-OCT images and to perform analysis on specific structures in the ONH. Analysis of displacements and strains during the development of experimental glaucoma was performed in the LC and peripheral RNFL. We observed that persistent high IOP, resulted from glaucoma, generates strain in the ONH and such strain settles down with time. The LC tended to be less mechanically stable under chronic IOP elevation compared to the peripheral part of the retinal nerve fiber layer. Large deformation was observed in the LC soon after the laser photocoagulation. Stretch, compression and shear did not necessarily increase at the same time, nor necessarily colocalize in the 3D strain map. Furthermore, strains in the ONH did not strictly follow the trend of IOP elevations over time, confirming the distinction between acute and chronic IOP elevations. This is the first study that applies the DVC technique to study the mechanics of the ONH on a dataset that spans the whole process of the glaucoma development. The tools developed in this project enable us to interpret the data and to understand the pathophysiology of glaucoma.

# 6.0 Future Work

## 6.1 Further Improvement of the DVC Accuracy

The accuracy of the DVC program can be further improved. In the current project, limited by the computing power and algorithm efficiency, the location of peak correlation was calculated by the index of the largest element in the correlation matrix. When searching for the best match point in the deformed image based on the ZNCC, the real peak correlation does not have to, and most likely will not, occur at a position with integer coordinates. So, a better method is to consider it as an unconstrained non-linear optimization problem where the objective is to find the maximum of a function whose values at integer coordinates were defined by the correlation matrix. Suitable quasi-newton's method can be used to solve the optimization problem and to achieve sub-voxel accuracy in the displacement computation. However, this method is computationally heavy. Potential future work includes implementing a more efficient algorithm to solve the optimization problem, as well as to improve the efficiency of other parts of the DVC program, to make it feasible to achieve sub-voxel accuracy in reasonable run time.

Furthermore, we have observed that the performance is not as good when applying the DVC program to images with large deformations, i.e., cumulative deformations from baseline to late stages of experimental glaucoma. Due to this limitation, a cumulative, in other words "all to baseline", analysis was not performed in this project but could be very interesting to look at. These improvements will be incorporated in the future. Potential ways to overcome this technical challenge include adding displacement vectors calculated in the stepwise analysis to obtain the cumulative displacements (Pyne et al., 2014) and improving the sampling and meshing algorithms

as well as the searching algorithms to detect larger displacements. We expect the later one to be a better approach for our application because the former method could cause error to accumulate during the addition of the displacement vectors and will be very computationally heavy.

### 6.2 Analyze More Regions in the Optic Nerve Head

In this project, the focus was to develop the tools and methods for analyzing 3D deformations in OCT images. Two structures were segmented from the image volumes and were analyzed. Next steps of this project are to apply the developed tools to segment more regions of interest, e.g., the central retinal nerve fiber layer and the neuro-retinal rim area, which are also regions of neural tissue loss in glaucoma.

### 6.3 Tissue Response to Acute IOP Elevations at Different Phases of Glaucoma

In this initial study, we only analyzed the OCT scans obtained at normal IOP. The full data set also includes scans at multiple IOPs. These scans capture the tissues response to increased IOP at different stages of experimental glaucoma. A next step of this project would be analyzing these scans with increased pressure. By measuring the deformation of the tissues under different pressures, we will be able to gain insights on the mechanical behavior of the tissue and how tissues' mechanical properties change as glaucoma progresses.

### 6.4 Implement the Appropriate Statistical Analysis, Control Eyes and Larger Sample Sizes

Crucial to the future application of this tool is the integration with appropriate statistical analysis methods. The techniques will potentially be related to mixed effects models, but will require careful attention to difficult challenges, including: spatial autocorrelation in the measurements, sampling issues in which different tissue regions may be measured at each condition, use of contralateral eyes as pseudo-controls to characterize variability and systemic issues such as inflammation. In this work, the scans before the first laser can approximate a control. Future work should also extend the study to a much larger sample size. In this work we focused on a single eye due to the challenges of developing the tools themselves.

# Appendix A Additionnal Figures for All Scans

## Appendix A.1 Displacement Verification

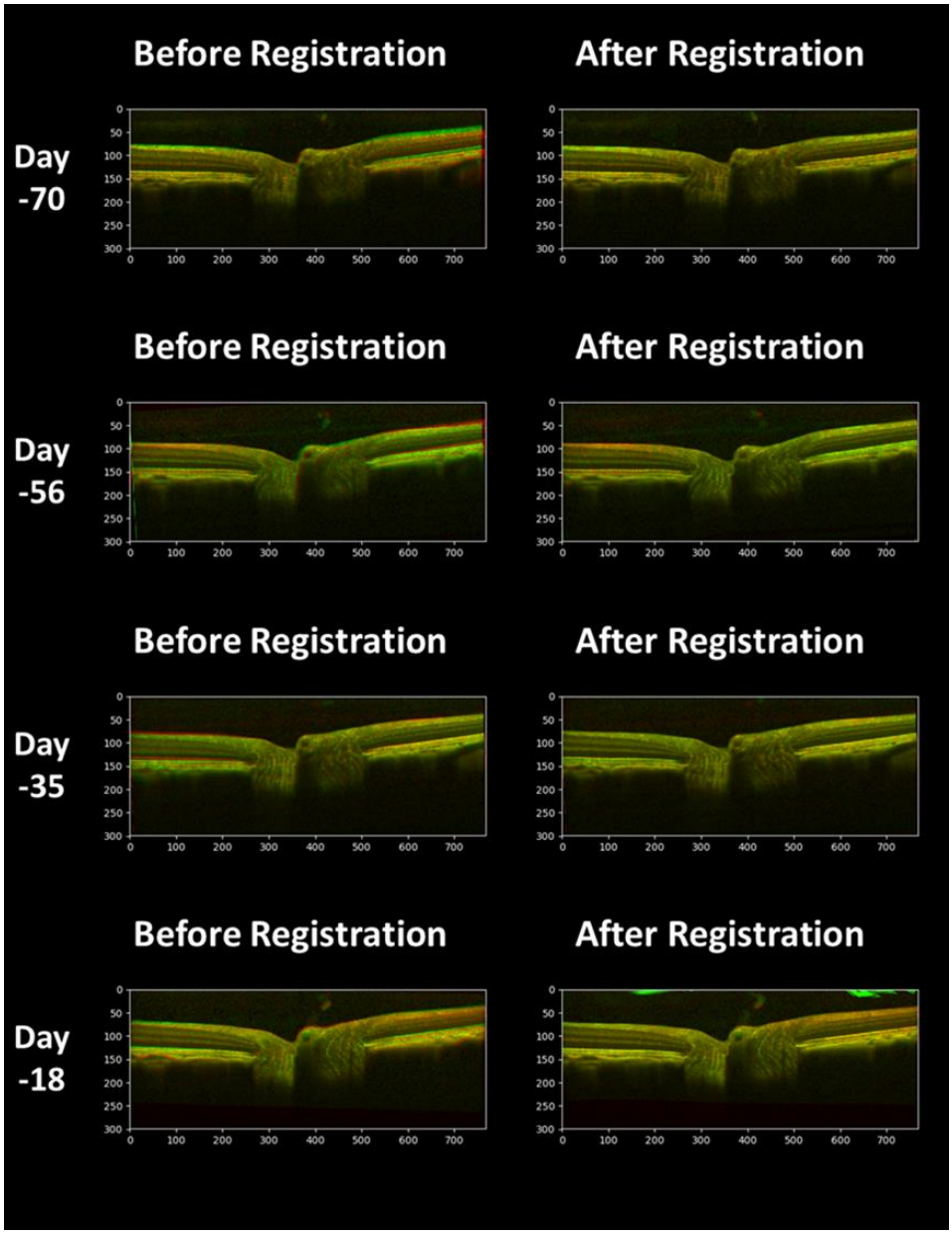


**Appendix Figure 1. Displacement verification for all scans (a)**

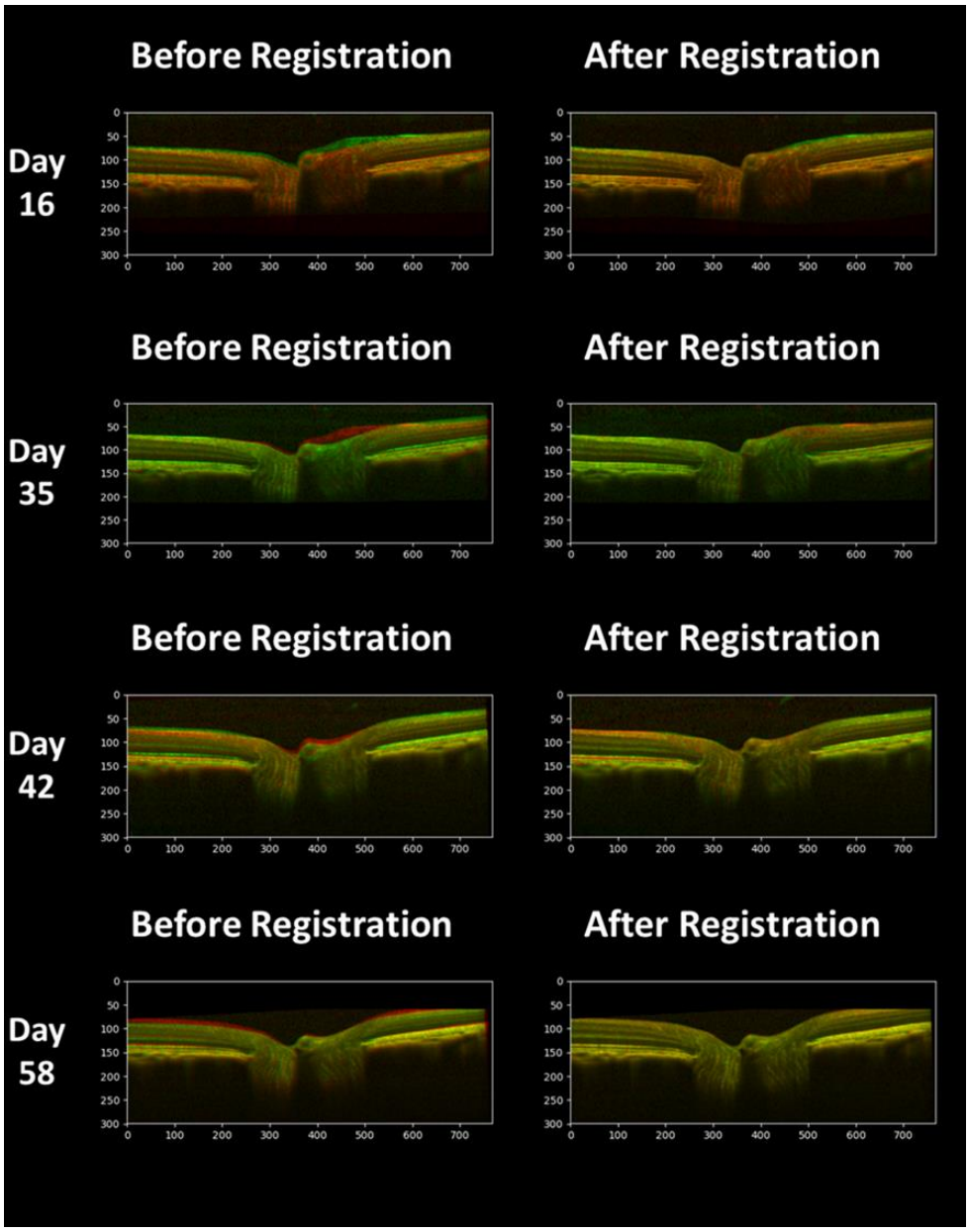


**Appendix Figure 2. Displacement verification for all scans (b)**

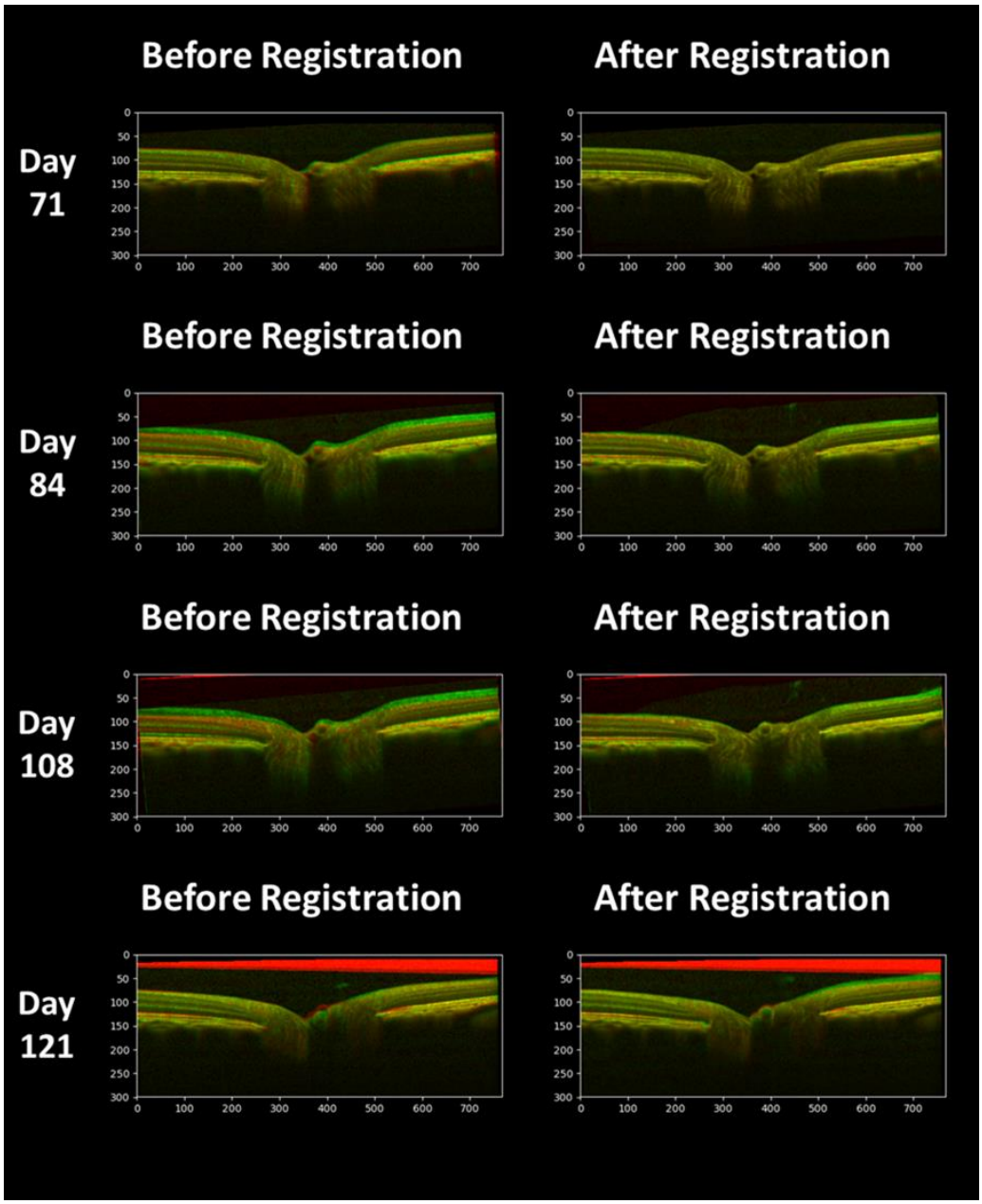


**Appendix Figure 3. Displacement verification for all scans (c)**

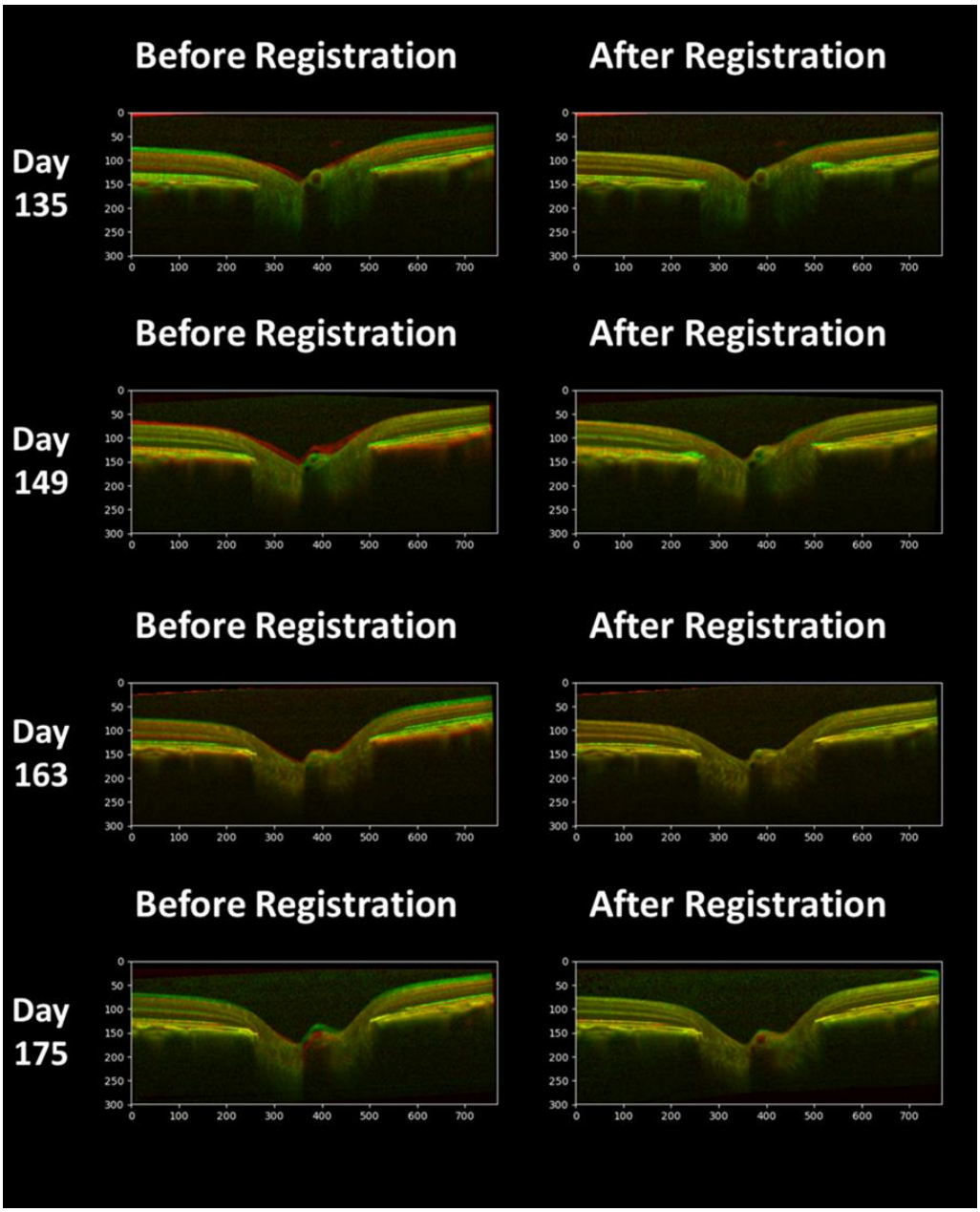


**Appendix Figure 4. Displacement verification for all scans (d)**

## Appendix A.2 Strain Results

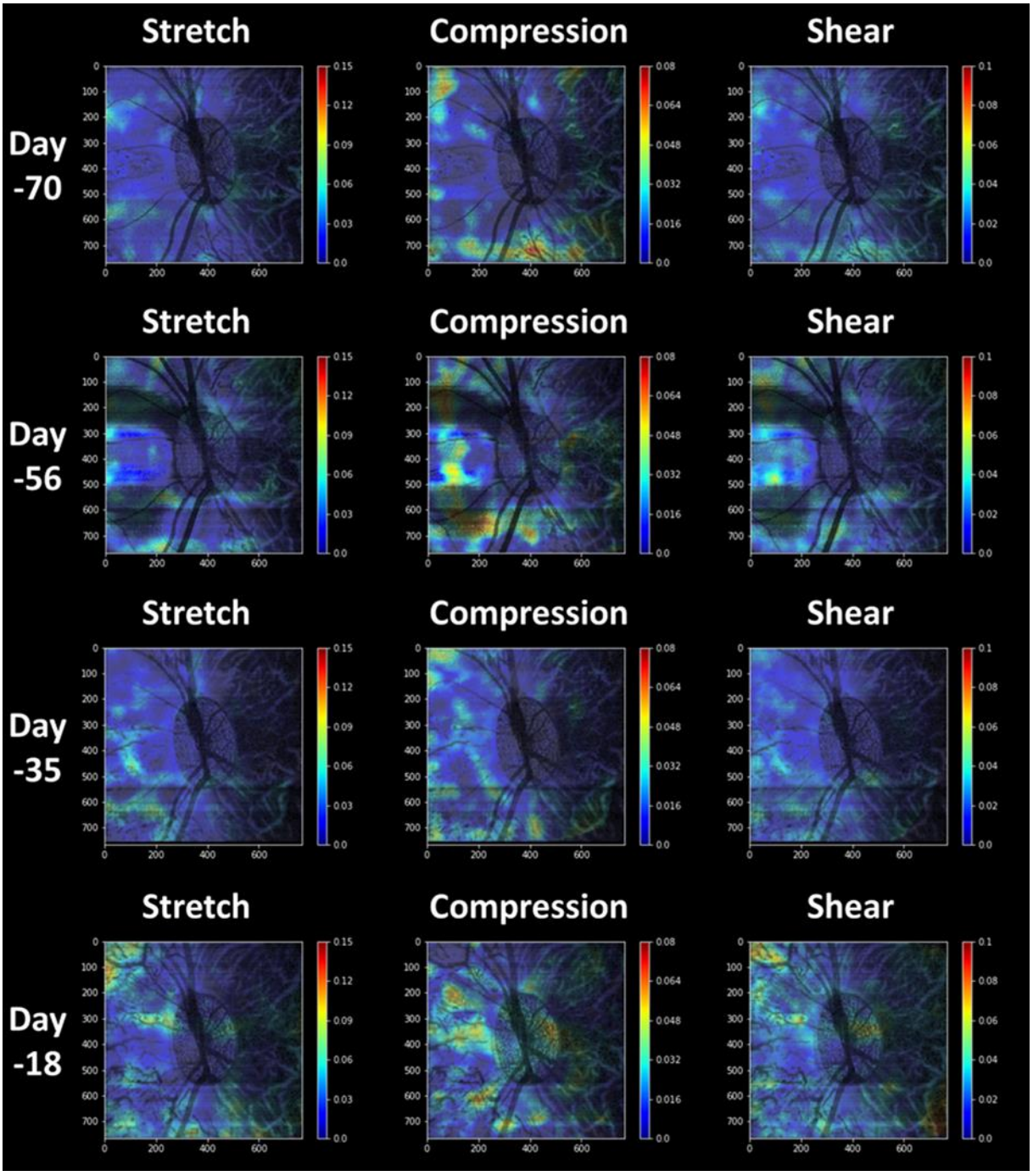


**Appendix Figure 5. Stretch, compression and shear strain for all scans. (a)**

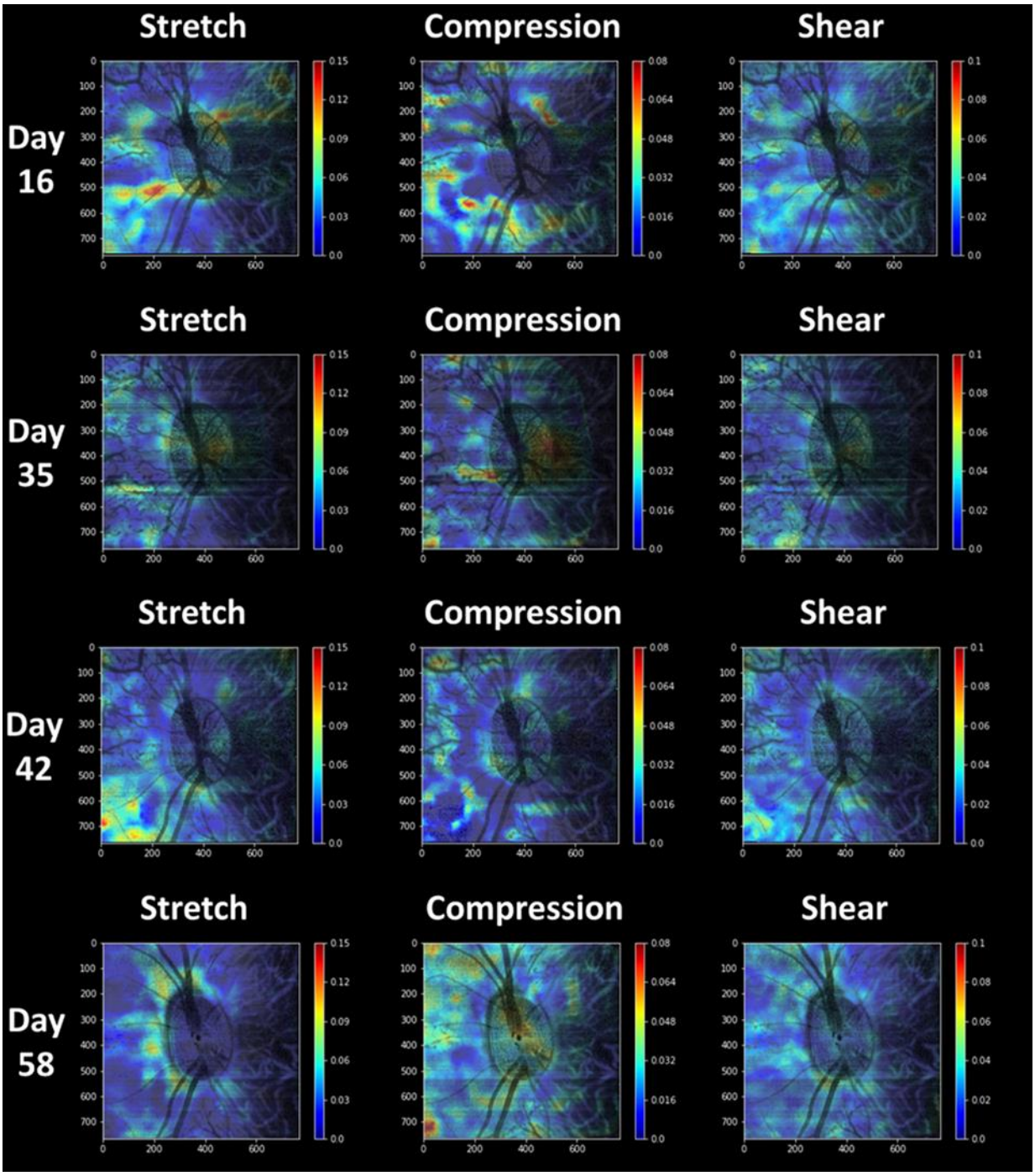


**Appendix Figure 6. Stretch, compression and shear strain for all scans. (b)**

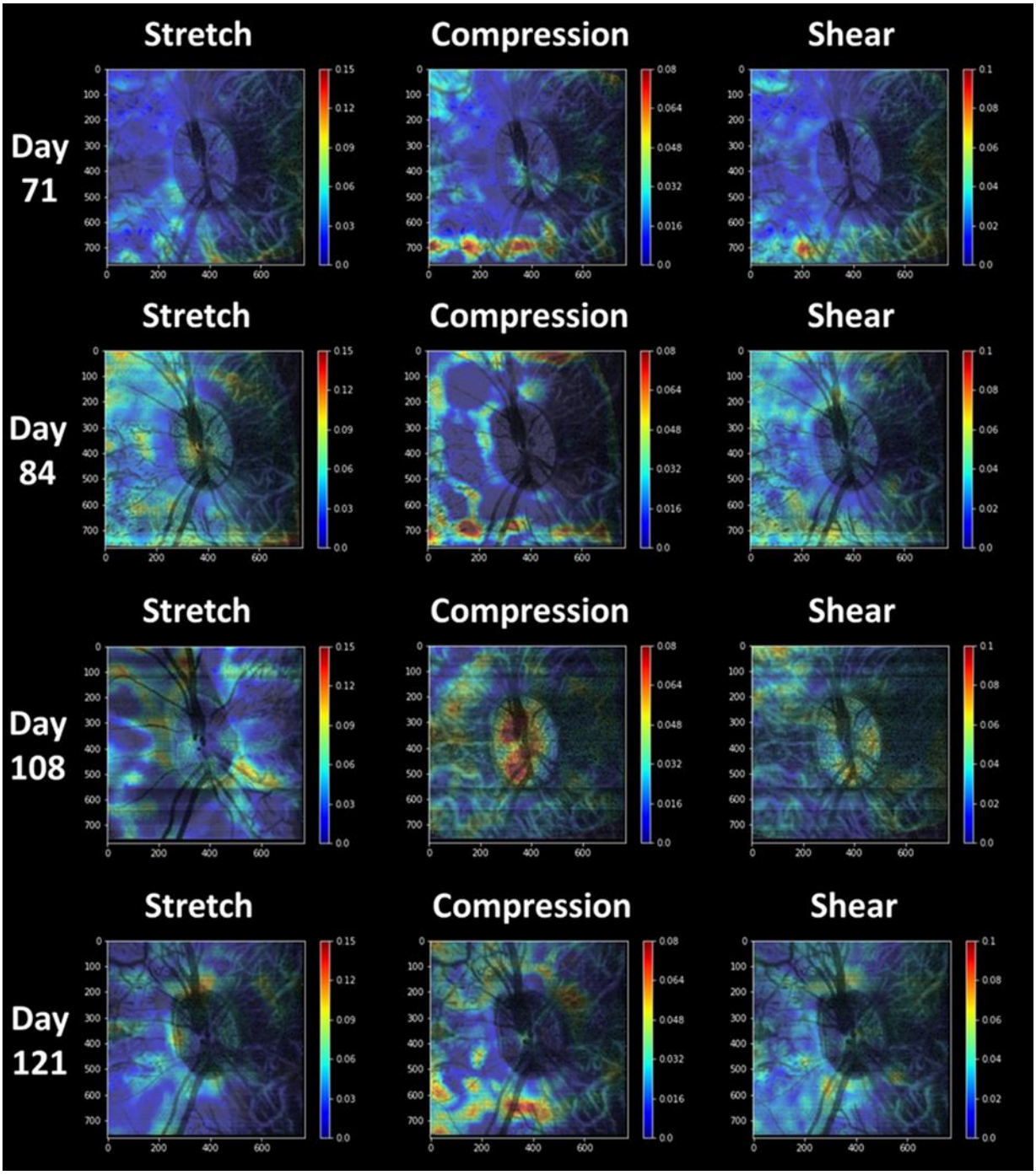


**Appendix Figure 7. Stretch, compression and shear strain for all scans. (c)**

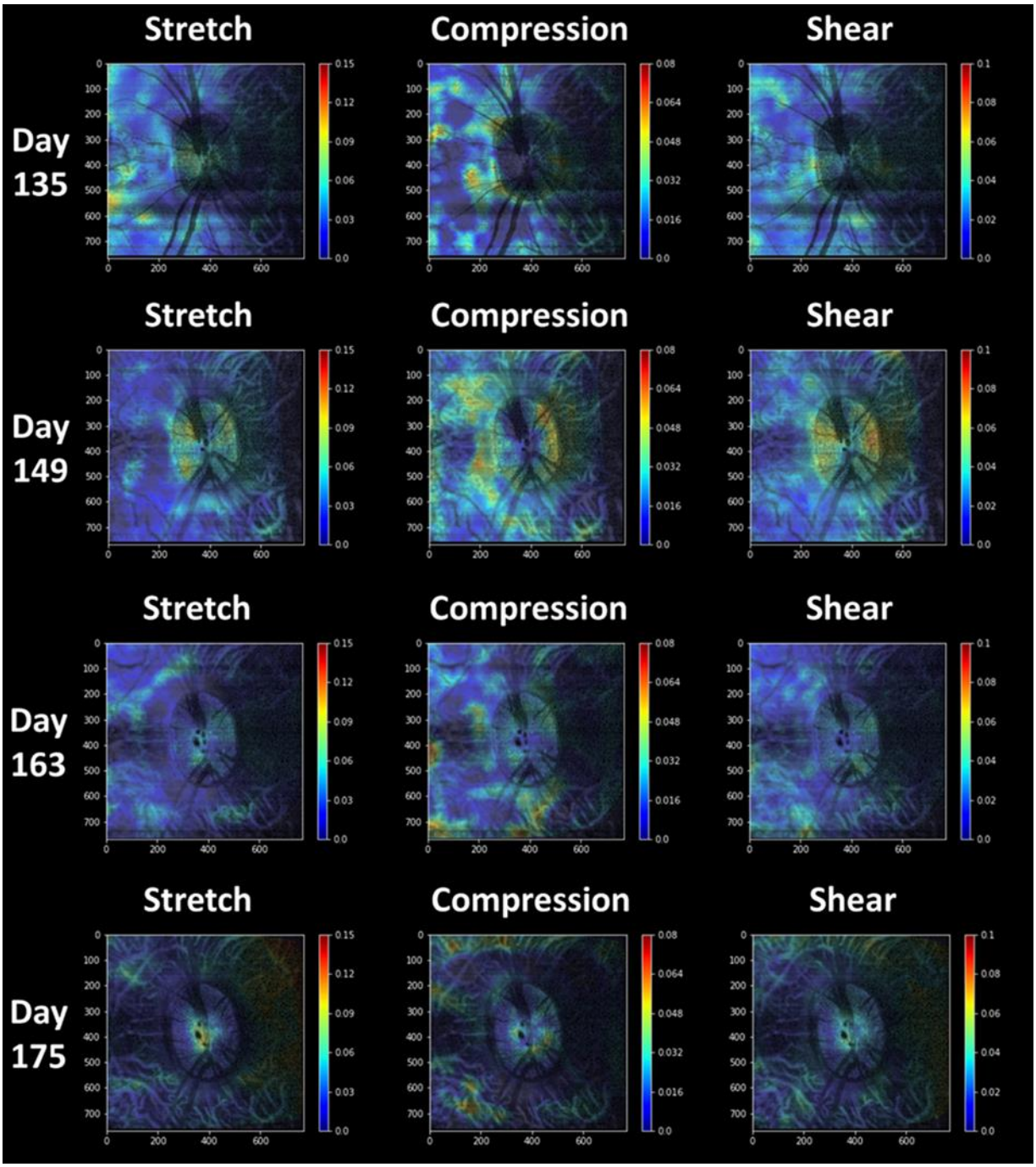


**Appendix Figure 8. Stretch, compression and shear strain for all scans. (d)**

## Appendix A.3 Strain Distribution Ridge Plots

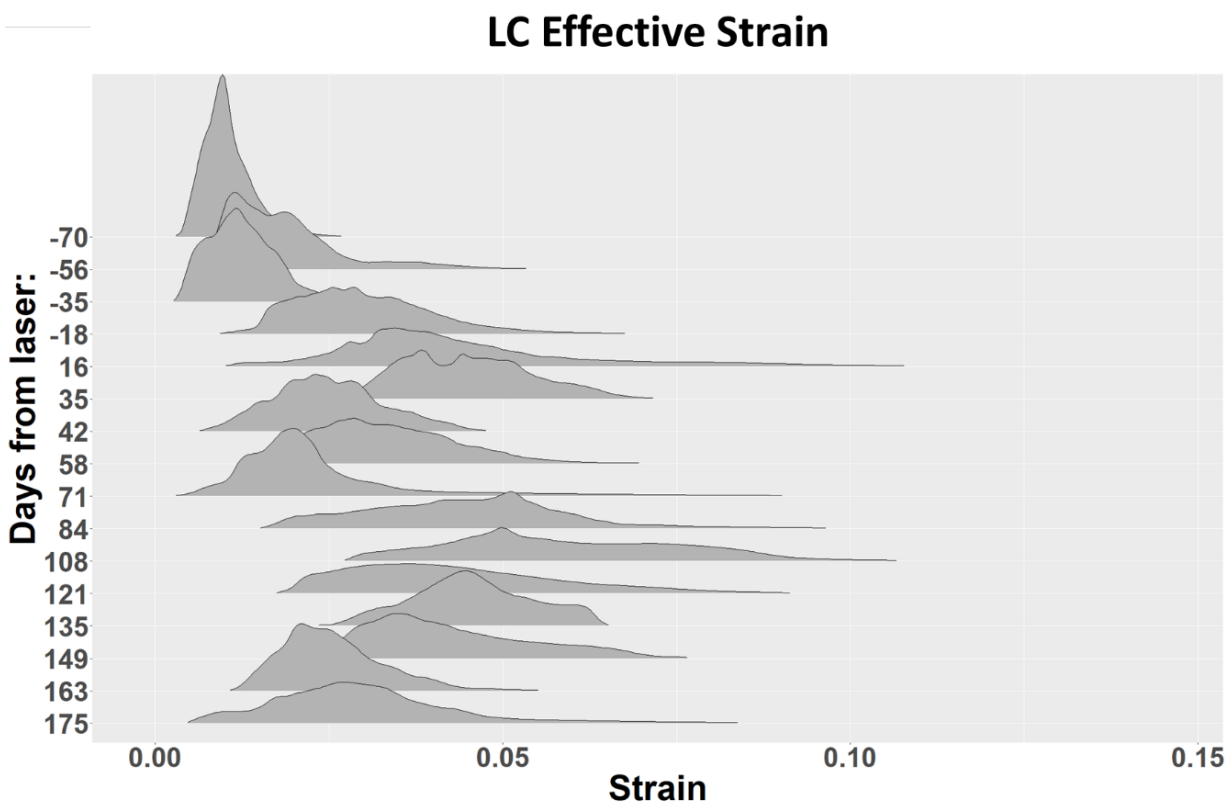


**Appendix Figure 9. Ridge plot of the LC effective strain.**

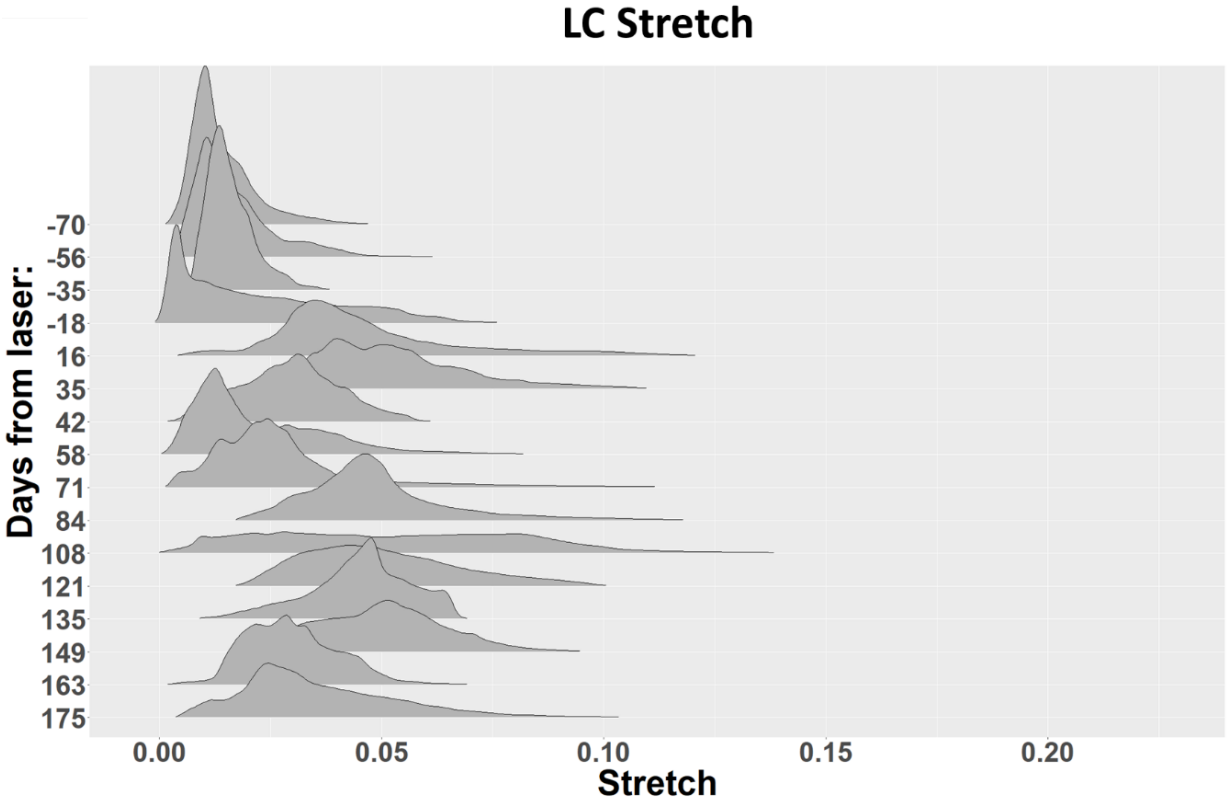


**Appendix Figure 10. Ridge plot of the LC stretch.**

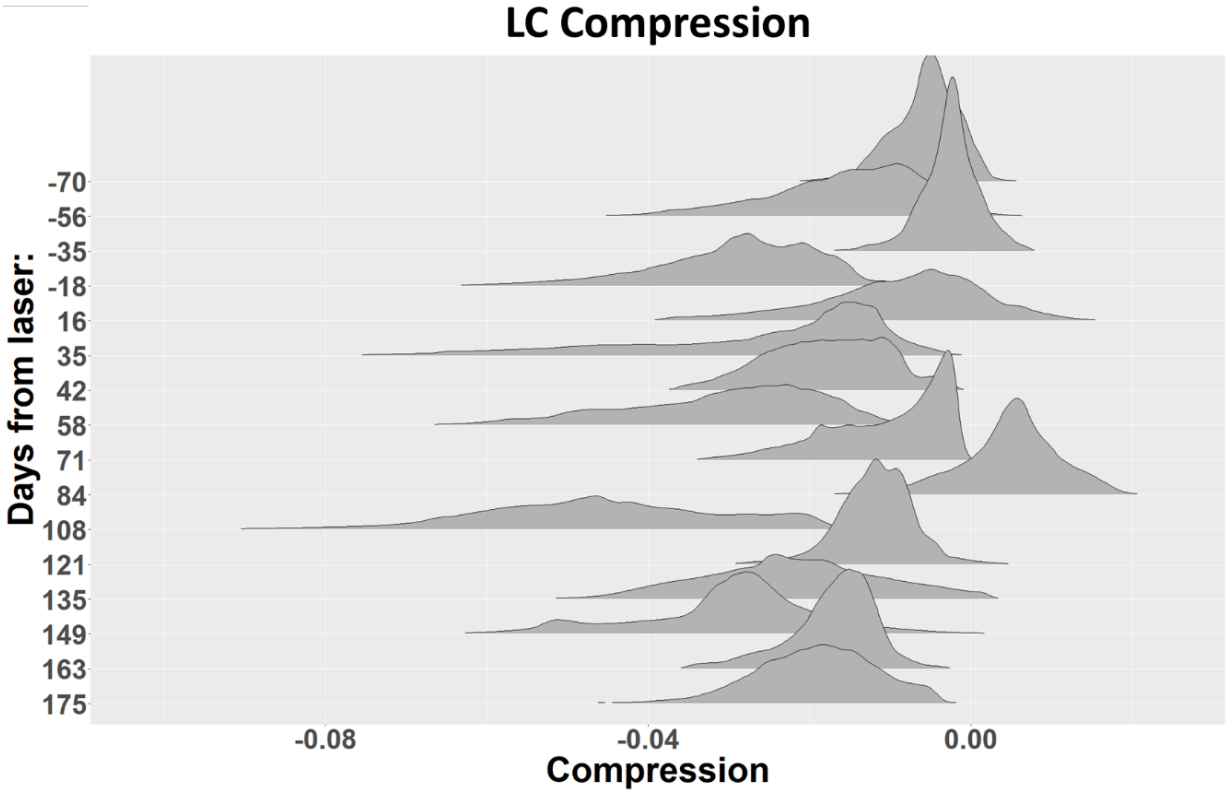


**Appendix Figure 11. Ridge plot of the LC compression.**

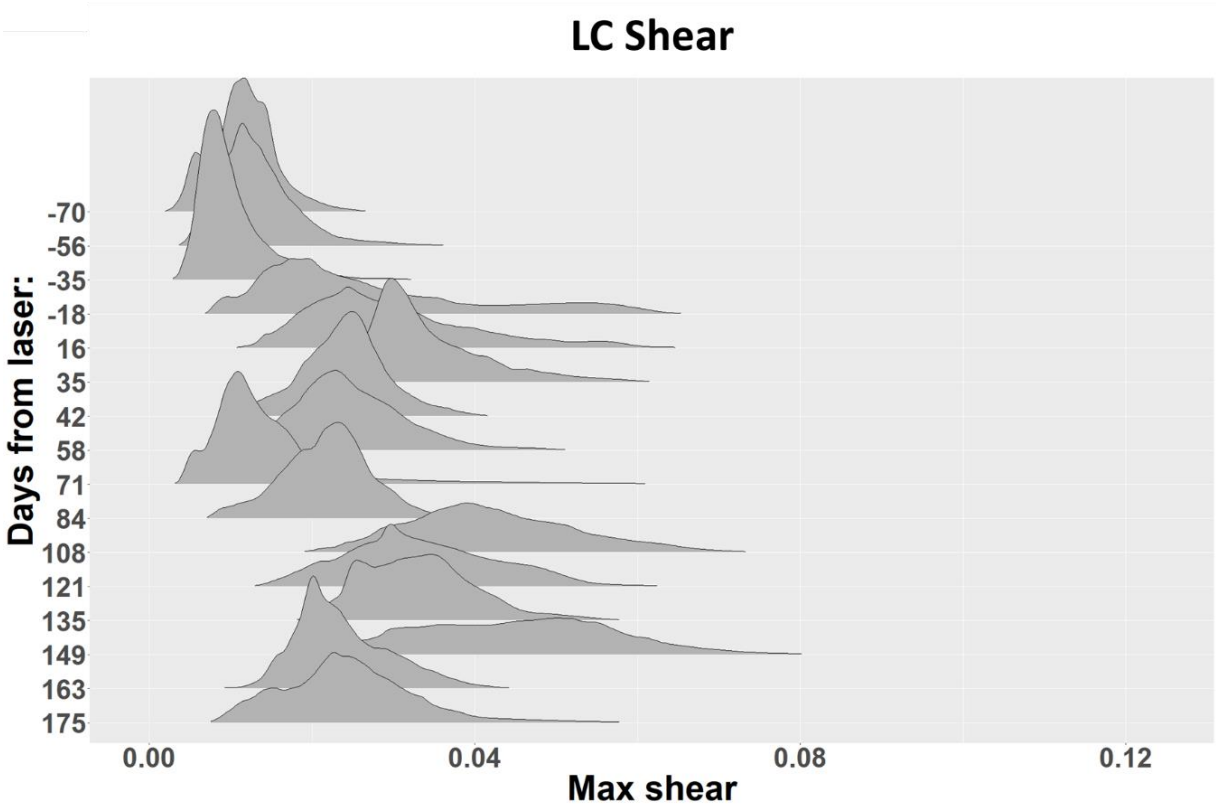


**Appendix Figure 12. Ridge plot of the LC shear strain.**

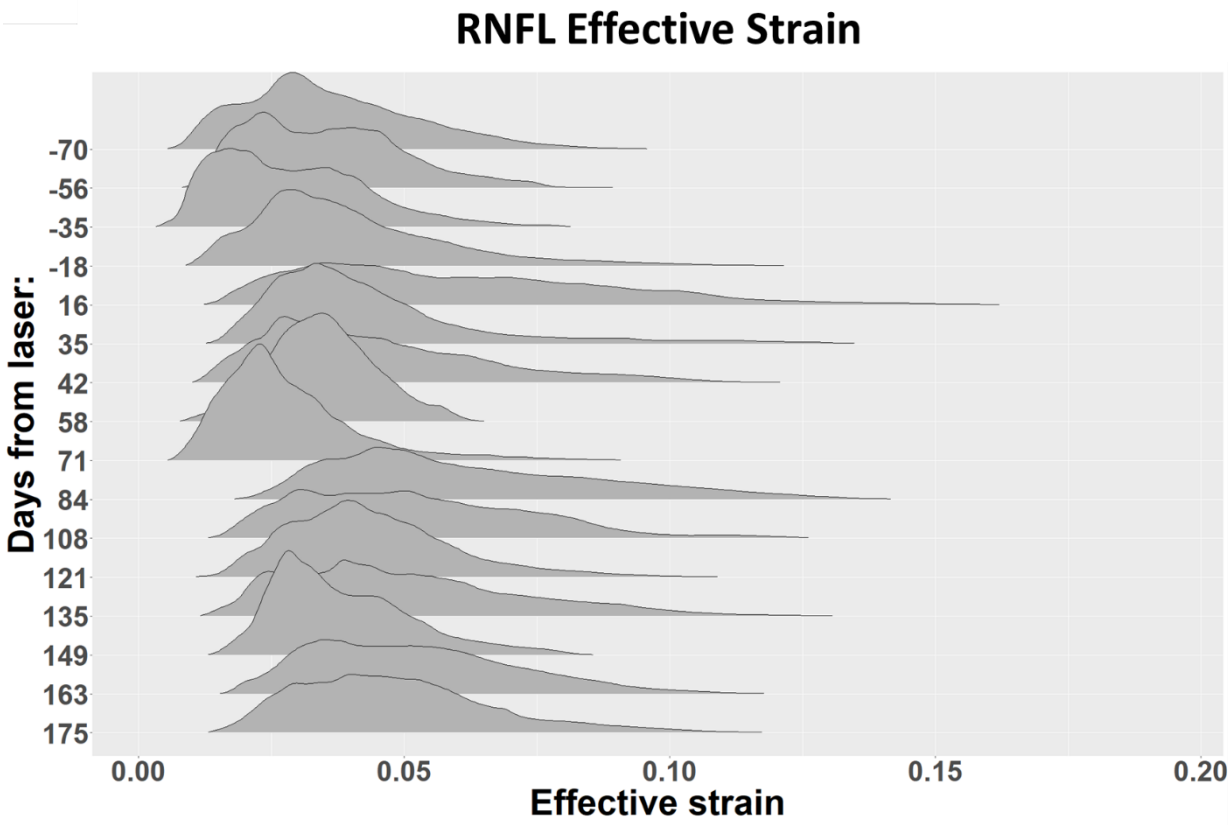


**Appendix Figure 13. Ridge plot of the RNFL effective strain.**

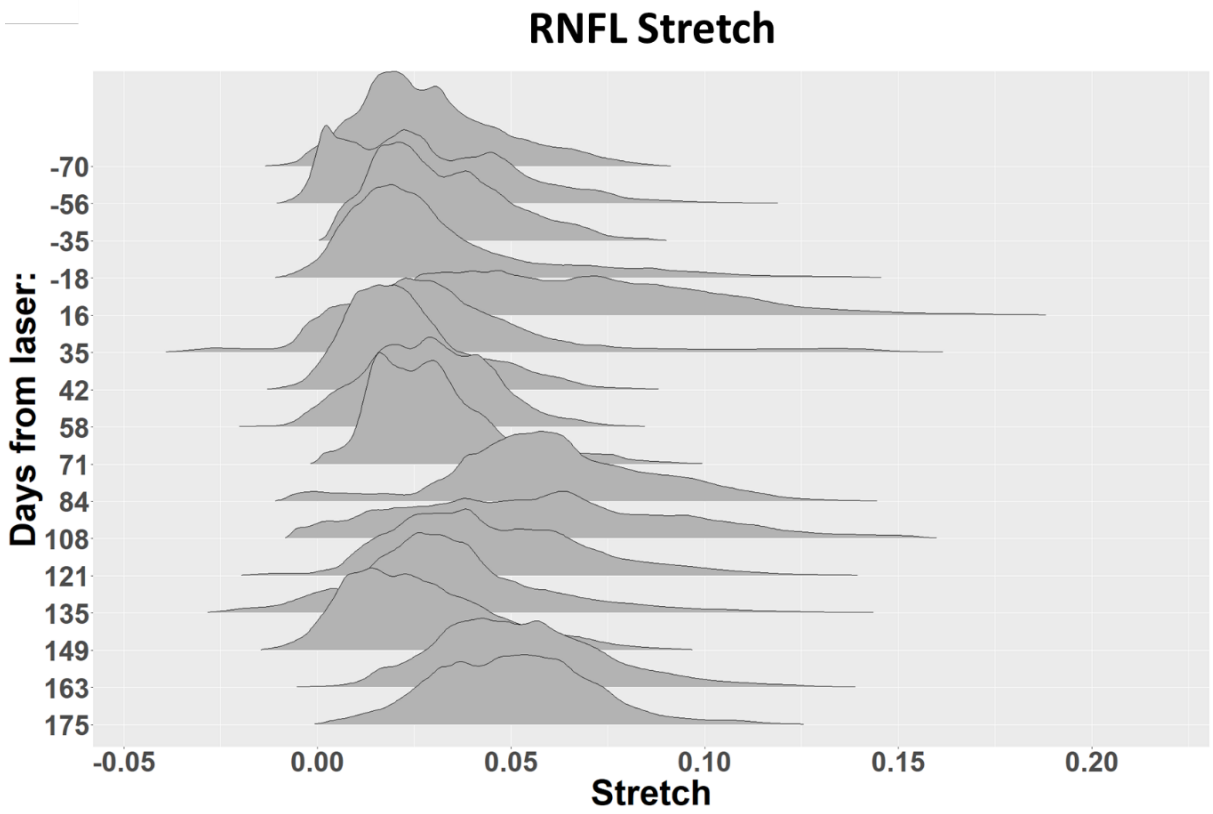


**Appendix Figure 14. Ridge plot of the RNFL stretch.**

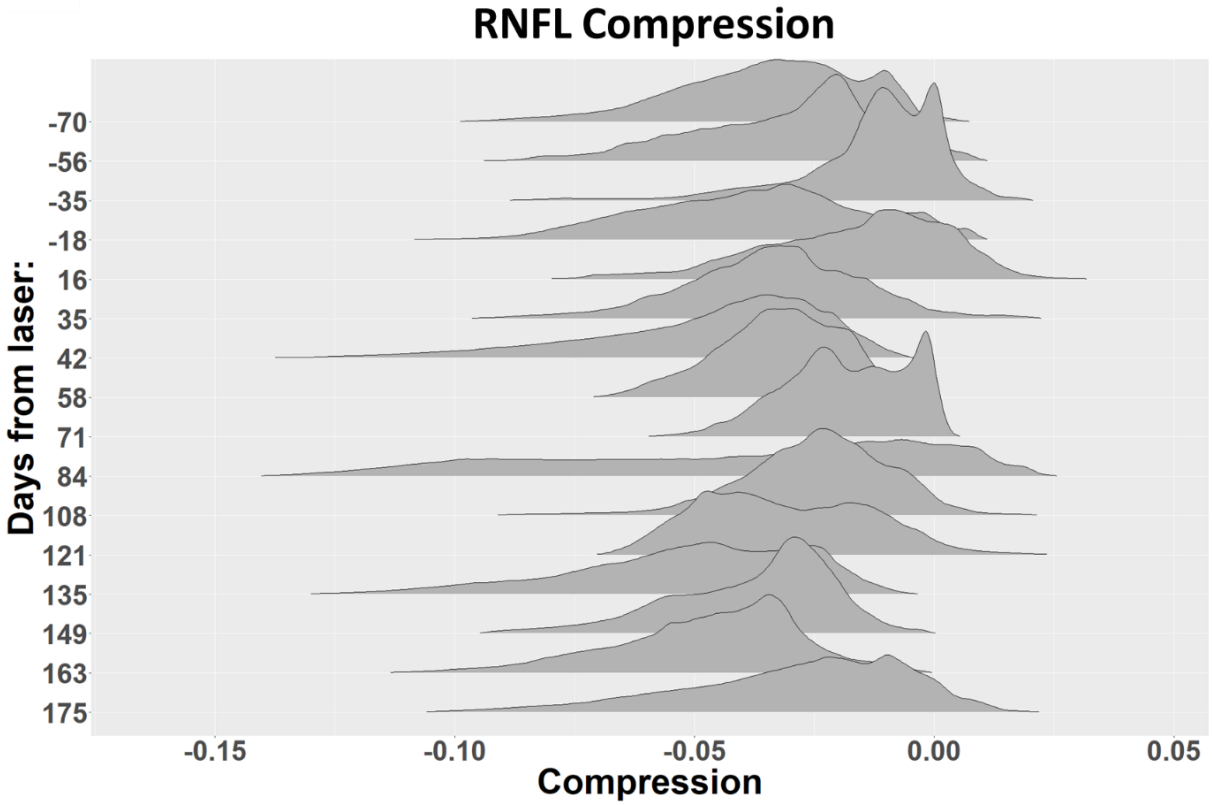


**Appendix Figure 15. Ridge plot of the RNFL compression.**

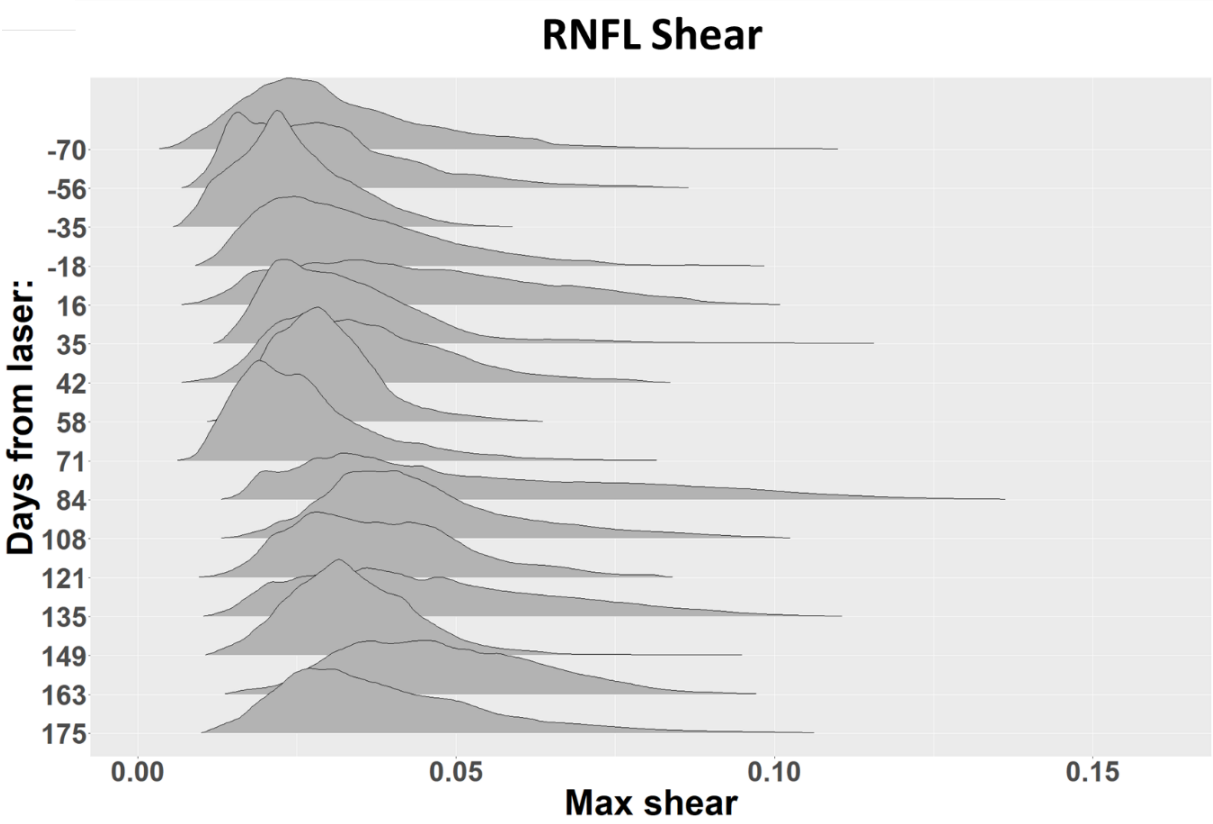


**Appendix Figure 16. Ridge plot of the RNFL shear strain.**

## Bibliography


Balaratnasingam, C., Kang, M. H., Yu, P., Chan, G., Morgan, W. H., Cringle, S. J., & Yu, D. Y. (2014). Comparative quantitative study of astrocytes and capillary distribution in optic nerve laminar regions. *Experimental Eye Research*, *121*, 11–22. https://doi.org/10.1016/j.exer.2014.02.008

Bay, B. K., Smith, T. S., Fyhrie, D. P., & Saad, M. (1999). Digital volume correlation: Three-dimensional strain mapping using x-ray tomography. *Experimental Mechanics*, *39*(3), 217–226. https://doi.org/10.1007/BF02323555

Behkam, R., Kollech, H. G., Jana, A., Hill, A., Danford, F., Howerton, S., Ram, S., Rodríguez, J. J., Utzinger, U., Girkin, C. A., & Vande Geest, J. P. (2019). Racioethnic differences in the biomechanical response of the lamina cribrosa. *Acta Biomaterialia*, *88*, 131–140. https://doi.org/10.1016/j.actbio.2019.02.028

Burgoyne, C. F., Crawford Downs, J., Bellezza, A. J., Francis Suh, J. K., & Hart, R. T. (2005). The optic nerve head as a biomechanical structure: A new paradigm for understanding the role of IOP-related stress and strain in the pathophysiology of glaucomatous optic nerve head damage. In *Progress in Retinal and Eye Research* (Vol. 24, Issue 1, pp. 39–73). https://doi.org/10.1016/j.preteyeres.2004.06.001

Burgoyne, C. F., Downs, J. C., Bellezza, A. J., & Hart, R. T. (2004). Three-dimensional reconstruction of normal and early glaucoma monkey optic nerve head connective tissues. *Investigative Ophthalmology and Visual Science*, *45*(12), 4388–4399. https://doi.org/10.1167/iovs.04-0022

Campbell, I. C., Coudrillier, B., & Ross Ethier, C. (2014). Biomechanics of the posterior eye: a critical role in health and disease. *Journal of Biomechanical Engineering*, *136*(2), 021005. https://doi.org/10.1115/1.4026286

Chu, T. C., Ranson, W. F., & Sutton, M. A. (1985). Applications of digital-image-correlation techniques to experimental mechanics. *Experimental Mechanics*, *25*(3), 232–244. https://doi.org/10.1007/BF02325092

Crawford Downs, J., Roberts, M. D., & Sigal, I. A. (2011). Glaucomatous cupping of the lamina cribrosa: A review of the evidence for active progressive remodeling as a mechanism. *Experimental Eye Research*, *93*(2), 133–140. https://doi.org/10.1016/j.exer.2010.08.004

Dunbar, D., & Greg, H. (2004). A Spatial Data Structure for Fast Poisson-Disk Sample Generation. *Polyphenols Communications*, *2004*, 759–760.

Feola, A. J., Coudrillier, B., Mulvihill, J., Geraldes, D. M., Vo, N. T., Albon, J., Abel, R. L., Samuels, B. C., & Ethier, C. R. (2017). Deformation of the lamina cribrosa and optic nerve

due to changes in cerebrospinal fluid pressure. *Investigative Ophthalmology and Visual Science*, *58*(4), 2070–2078. https://doi.org/10.1167/iovs.16-21393

Fortune, B., Reynaud, J., Hardin, C., Wang, L., Sigal, I. A., & Burgoyne, C. F. (2016). Experimental glaucoma causes optic nerve head neural rim tissue compression: A potentially important mechanism of axon injury. *Investigative Ophthalmology and Visual Science*, *57*(10), 4403–4411. https://doi.org/10.1167/iovs.16-20000

Fortune, B., Yang, H., Strouthidis, N. G., Cull, G. A., Grimm, J. L., Downs, J. C., & Burgoyne, C. F. (2009). The effect of acute intraocular pressure elevation on peripapillary retinal thickness, retinal nerve fiber layer thickness, and retardance. *Investigative Ophthalmology and Visual Science*, *50*(10), 4719–4726. https://doi.org/10.1167/iovs.08-3289

Girard, Michael J.A., Strouthidis, N. G., Desjardins, A., Mari, J. M., Ethier, C. R., & Lyon, D. (2013). In vivo optic nerve head biomechanics : performance testing of a three- dimensional tracking algorithm. *Journal of The Royal Society Interface*, *10*(87), 20130459. http://dx.doi.org/10.1098/rsif.2013.0459

Girard, Michäel J.A., Tun, T. A., Husain, R., Acharyya, S., Haaland, B. A., Wei, X., Mari, J. M., Perera, S. A., Baskaran, M., Aung, T., & Strouthidis, N. G. (2015). Lamina cribrosa visibility using optical coherence tomography: Comparison of devices and effects of image enhancement techniques. *Investigative Ophthalmology and Visual Science*, *56*(2), 865–874. https://doi.org/10.1167/iovs.14-14903

Jonas, J. B., Königsreuther, K. A., & Naumann, G. O. H. (1992). Optic disc histomorphometry in normal eyes and eyes with secondary angle-closure glaucoma - II. Parapapillary region. *Graefe's Archive for Clinical and Experimental Ophthalmology*, *230*(2), 134–139. https://doi.org/10.1007/BF00164651

Lewis, J. P. (1995). Fast Template Matching, Vision Interface 95, Canadian Image Processing and Pattern Recognition Society. *Vision Interface*, *95*, 120–123. https://s3.amazonaws.com/academia.edu.documents/3607631/10.1.1.157.3888.pdf?AWSAccessKeyId=AKIAIWOWYYGZ2Y53UL3A&Expires=1538328118&Signature=l7BnOyfMzqaHU52mQBM7d6UTl3M%3D&response-content-disposition=inline%3Bfilename%3DFast_template_matching.pdf

Lucy, K. A., Wang, B., Schuman, J. S., Bilonick, R. A., Ling, Y., Kagemann, L., Sigal, I. A., Grulkowski, I., Liu, J. J., Fujimoto, J. G., Ishikawa, H., & Wollstein, G. (2017). Thick prelaminar tissue decreases lamina cribrosa visibility. *Investigative Ophthalmology and Visual Science*, *58*(3), 1751–1757. https://doi.org/10.1167/iovs.16-20784

Midgett, D. E., Pease, M. E., Jefferys, J. L., Patel, M., Franck, C., Quigley, H. A., & Nguyen, T. D. (2017). The pressure-induced deformation response of the human lamina cribrosa: Analysis of regional variations. *Acta Biomaterialia*, *53*, 123–139. https://doi.org/10.1016/j.actbio.2016.12.054

Midgett, D. E., Quigley, H. A., & Nguyen, T. D. (2019). In vivo characterization of the deformation of the human optic nerve head using optical coherence tomography and digital

volume correlation. *Acta Biomaterialia*, *96*, 385–399. https://doi.org/10.1016/j.actbio.2019.06.050

Pyne, J. D., Genovese, K., Casaletto, L., & Vande Geest, J. P. (2014). Sequential-digital image correlation for mapping human posterior sclera and optic nerve head deformation. *Journal of Biomechanical Engineering*, *136*(2), 0210021. https://doi.org/10.1115/1.4026224

Quigley, H A, & Broman, A. T. (2006). The number of people with glaucoma worldwide in 2010 and 2020. *The British Journal of Ophthalmology*, *90*(3), 262–267. https://doi.org/10.1136/bjo.2005.081224

Quigley, Harry A., Hohman, R. M., Addicks, E. M., Massof, R. W., & Richard Green, W. (1983). Morphologic changes in the lamina cribrosa correlated with neural loss in open-angle glaucoma. *American Journal of Ophthalmology*, *95*(5), 673–691. https://doi.org/10.1016/0002-9394(83)90389-6

Reddy, B. S., & Chatterji, B. N. (1996). An FFT-Based Technique for Translation, Rotation, and Scale-Invariant Image Registration. In *IEEE TRANSACTIONS ON IMAGE PROCESSING* (Vol. 5, Issue 8). http://www.lira.dist.unige.it/teaching/SINA_10/slides-current/fourier-mellin-paper.pdf

Rueden, C. T., Schindelin, J., Hiner, M. C., DeZonia, B. E., Walter, A. E., Arena, E. T., & Eliceiri, K. W. (2017). ImageJ2: ImageJ for the next generation of scientific image data. *BMC Bioinformatics*, *18*(1), 529. https://doi.org/10.1186/s12859-017-1934-z

Saito, T., & Toriwaki, J. I. (1994). New algorithms for euclidean distance transformation of an n-dimensional digitized picture with applications. *Pattern Recognition*, *27*(11), 1551–1565. https://doi.org/10.1016/0031-3203(94)90133-3

Schindelin, J., Arganda-Carreras, I., Frise, E., Kaynig, V., Longair, M., Pietzsch, T., Preibisch, S., Rueden, C., Saalfeld, S., Schmid, B., Tinevez, J. Y., White, D. J., Hartenstein, V., Eliceiri, K., Tomancak, P., & Cardona, A. (2012). Fiji: An open-source platform for biological-image analysis. In *Nature Methods* (Vol. 9, Issue 7, pp. 676–682). Nature Publishing Group. https://doi.org/10.1038/nmeth.2019

Sigal, I. A., Flanagan, J. G., Lathrop, K. L., Tertinegg, I., & Bilonick, R. (2012). Human lamina cribrosa insertion and age. *Investigative Ophthalmology and Visual Science*, *53*(11), 6870–6879. https://doi.org/10.1167/iovs.12-9890

Sigal, I. A., Grimm, J. L., Jan, N. J., Reid, K., Minckler, D. S., & Brown, D. J. (2014). Eye-specific iop-induced displacements and deformations of human lamina cribrosa. *Investigative Ophthalmology and Visual Science*, *55*(1), 1–15. https://doi.org/10.1167/iovs.13-12724

Sigal, I. A., Schuman, J. S., Ishikawa, H., Kagemann, L., & Wollstein, G. (2016). A problem of proportions in Oct-based morphometry and a proposed solution. In *Investigative Ophthalmology and Visual Science* (Vol. 57, Issue 2, pp. 484–485). Association for Research in Vision and Ophthalmology Inc. https://doi.org/10.1167/iovs.15-18570

Sigal, I. A., Wang, B., Strouthidis, N. G., Akagi, T., & Girard, M. J. A. (2014). Recent advances in OCT imaging of the lamina cribrosa. In *British Journal of Ophthalmology* (Vol. 98, Issue SUPPL. 2, pp. ii34-9). BMJ Publishing Group. https://doi.org/10.1136/bjophthalmol-2013-304751

Sommer, A., Tielsch, J. M., Katz, J., Quigley, H. A., Gottsch, J. D., Javitt, J., & Singh, K. (1991). Relationship Between Intraocular Pressure and Primary Open Angle Glaucoma Among White and Black Americans: The Baltimore Eye Survey. *Archives of Ophthalmology*, *109*(8), 1090–1095. https://doi.org/10.1001/archopht.1991.01080080050026

Strouthidis, N. G., Fortune, B., Yang, H., Sigal, I. A., & Burgoyne, C. F. (2011a). Effect of acute intraocular pressure elevation on the monkey optic nerve head as detected by spectral domain optical coherence tomography. *Investigative Ophthalmology and Visual Science*, *52*(13), 9431–9437. https://doi.org/10.1167/iovs.11-7922

Strouthidis, N. G., Fortune, B., Yang, H., Sigal, I. a, & Burgoyne, C. F. (2011b). Longitudinal change detected by spectral domain optical coherence tomography in the optic nerve head and peripapillary retina in experimental glaucoma. *Investigative Ophthalmology & Visual Science*, *52*(3), 1206–1219. https://doi.org/10.1167/iovs.10-5599

Tamimi, E. A., Pyne, J. D., Muli, D. K., Axman, K. F., Howerton, S. J., Davis, M. R., Girkin, C. A., & Vande Geest, J. P. (2017). Racioethnic differences in human posterior scleral and optic nerve stump deformation. *Investigative Ophthalmology and Visual Science*, *58*(10), 4235–4246. https://doi.org/10.1167/iovs.17-22141

Van Der Walt, S., Schönberger, J. L., Nunez-Iglesias, J., Boulogne, F., Warner, J. D., Yager, N., Gouillart, E., & Yu, T. (2014). Scikit-image: Image processing in python. *PeerJ*, *2014*(1), e453. https://doi.org/10.7717/peerj.453

Virtanen, P., Gommers, R., Oliphant, T. E., Haberland, M., Reddy, T., Cournapeau, D., Burovski, E., Peterson, P., Weckesser, W., Bright, J., van der Walt, S. J., Brett, M., Wilson, J., Millman, K. J., Mayorov, N., Nelson, A. R. J., Jones, E., Kern, R., Larson, E., … Vázquez-Baeza, Y. (2020). SciPy 1.0: fundamental algorithms for scientific computing in Python. *Nature Methods*, *17*(3), 261–272. https://doi.org/10.1038/s41592-019-0686-2

Wei, J., Yang, B., Voorhees, A., Tran, H., Wang, B., Schuman, J., Wollstein, G., Smith, M., Brazile, B., & Sigal, I. A. (2018). Measuring in-vivo and in-situ ex-vivo the 3D deformation of the lamina cribrosa microstructure under elevated intraocular pressure. In K. V. Larin & D. D. Sampson (Eds.), *Optical Elastography and Tissue Biomechanics V* (Vol. 10496, p. 36). SPIE. https://doi.org/10.1117/12.2291243

Yang, H., Downs, J. C., Girkin, C., Sakata, L., Bellezza, A., Thompson, H., & Burgoyne, C. F. (2007). 3-D histomorphometry of the normal and early glaucomatous monkey optic nerve head: Lamina cribrosa and peripapillary scleral position and thickness. *Investigative Ophthalmology and Visual Science*, *48*(10), 4597–4607. https://doi.org/10.1167/iovs.07-0349

Yang, H., Ren, R., Lockwood, H., Williams, G., Libertiaux, V., Downs, C., Gardiner, S. K., & Burgoyne, C. F. (2015). The connective tissue components of optic nerve head cupping in monkey experimental glaucoma part 1: Global change. *Investigative Ophthalmology and Visual Science*, *56*(13), 7661–7678. https://doi.org/10.1167/iovs.15-17624

Zhang, L., Thakku, S. G., Beotra, M. R., Baskaran, M., Aung, T., Goh, J. C. H., Strouthidis, N. G., & Girard, M. J. A. (2017). Verification of a virtual fields method to extract the mechanical properties of human optic nerve head tissues in vivo. *Biomechanics and Modeling in Mechanobiology*, *16*(3), 871–887. https://doi.org/10.1007/s10237-016-0858-2